

# OPTICAL AND NEAR-IR IMAGING OF ULTRA STEEP SPECTRUM RADIO SOURCES - THE $K - Z$ DIAGRAM OF RADIO AND OPTICALLY SELECTED GALAXIES. <sup>1</sup>

CARLOS DE BREUCK<sup>2,3,4,5</sup>, WIL VAN BREUGEL<sup>4</sup>, S. A. STANFORD<sup>4,6</sup>

HUUB RÖTTGERING<sup>5</sup>, GEORGE MILEY<sup>5</sup>, DANIEL STERN<sup>7,8</sup>  
 debreuck@iap.fr, wil@igpp.ucllnl.org, adam@igpp.ucllnl.org, rottgeri@strw.leidenuniv.nl, miley@strw.leidenuniv.nl,  
 stern@zwolfkinder.jpl.nasa.gov

*To appear in the January 2002 Astronomical Journal*

## ABSTRACT

We present optical and/or near-IR images of 128 ultra steep spectrum (USS) radio sources. Roughly half of the objects are identified in the optical images ( $R \lesssim 24$ ), while in the near-IR images,  $>94\%$  are detected at  $K \lesssim 22$ . The mean  $K$ -magnitude is  $\bar{K} = 19.26$  within a  $2''$  diameter aperture. The distribution of  $R - K$  colors indicates that at least  $1/3$  of the objects observed have very red colors ( $R - K > 5$ ). The major axes of the identifications in  $K$ -band are preferentially oriented along the radio axes, with half of them having compact morphologies.

The 22 sources with spectroscopic redshifts and  $K$ -band magnitudes follow the  $K - z$  relation found from previous radio samples, but with a larger scatter. We argue that this may be due to a dependence of  $K$ -magnitude on the radio power, with the highest radio power sources inhabiting the most massive host galaxies. We present a composite  $K - z$  diagram of radio-loud and radio-quiet galaxies, selected from the HDF-North and the Hawaii surveys. Out to  $z \lesssim 1$ , the radio-loud galaxies trace the bright envelope of the radio quiet galaxies, while at  $z \gtrsim 1$ , the radio-loud galaxies are  $\gtrsim 2$  magnitudes brighter. We argue that this is not due to a contribution from the AGN or emission lines. This difference strongly suggests that radio galaxies pinpoint the most massive systems out to the highest known redshifts, probably due to the mutual correlation of the mass of the galaxy and the radio power on the mass of the central black hole.

*Subject headings:* Galaxies: active — radio continuum: galaxies — surveys — Cosmology: galaxy formation — galaxies: photometry — galaxies: structure — pulsars

## 1. INTRODUCTION

High redshift radio galaxies (HzRGs) provide some of the best opportunities to study the spatially resolved emission in galaxies out to the highest redshifts ( $z = 5.19$ ; van Breugel et al. 1999). Although they are no longer the only class of galaxies detected at such redshifts (*e.g.* Steidel et al. 1999; Spinrad et al. 1998; Weyman et al. 1998), they are still amongst the most massive forming galaxies known. Evidence that HzRGs are indeed massive galaxies in early phases of their formation is based on several observations. First of all, at low redshift ( $z \lesssim 1$ ), the host galaxies of powerful radio sources at are uniquely identified with massive ellipticals (*e.g.* Best, Longair, & Röttgering 1998; McLure & Dunlop 2000). Secondly, the tight correlation in the Hubble  $K - z$  diagram for powerful radio sources suggests that they may also be associated with such galaxies out to  $z \sim 5$  (*e.g.* Eales et al. 1997; van Breugel et al. 1998; Lacy, Bunker, & Ridgway 2000). Thirdly, many of the HzRGs consist of numerous components (van Breugel et al. 1998; Pentericci et al. 1999) *each* of which have sizes,  $UV_{rest}$  luminosities and star formation rates (SFRs) similar to the ‘Lyman Break galaxies’ galaxies found in field

surveys at  $z \sim 3 - 4$  (*e.g.* Steidel et al. 1999). Fourth, in at least two HzRGs there is direct, spectroscopic evidence for massive star formation based on stellar absorption-line spectra (Dey et al. 1997; Dey 1999a). Fifth, redshifted molecular (CO) lines (Papadopoulos et al. 2000) and sub-mm (Iverson et al. 1998; Archibald et al. 2001; Reuland et al. 2001) detections have been reported for many HzRGs: the inferred SFRs of  $\sim 1500 M_{\odot} \text{yr}^{-1}$  are sufficient to form massive galaxies if sustained over  $\sim 1$  Gyr.

Because HzRGs are more luminous and larger than field galaxies at similar redshifts, detailed studies of their optical and near-IR morphologies can be carried out. For example, deep  $K$ -band imaging (rest-frame optical) has indicated a morphological evolution in the host galaxies of the most powerful radio sources: at  $z \gtrsim 3$ , they display faint, large-scale morphologies, often surrounded by multiple components aligned with the radio source, while at  $z \lesssim 3$ , they appear as a single, compact structure without radio-aligned components (van Breugel et al. 1998, hereafter vB98). Using *HST/NICMOS*  $H$ -band data, Pentericci et al. (2001) found a similar change from objects with de Vaucouleurs profiles at  $z \leq 2.3$  to irregular at

<sup>2</sup> Institut d’Astrophysique de Paris, 98bis Boulevard Arago, 75014 Paris, France

<sup>3</sup> Marie Curie Fellow

<sup>4</sup> Institute of Geophysics and Planetary Physics, Lawrence Livermore National Laboratory, L-413, P.O. Box 808, Livermore, CA 94550, U.S.A.

<sup>5</sup> Leiden Observatory, P.O. Box 9513, 2300 RA Leiden, The Netherlands

<sup>6</sup> Physics Department, University of California, Davis, CA 95616, U.S.A.

<sup>7</sup> Astronomy Department, University of California at Berkeley, CA 94720, U.S.A.

<sup>8</sup> Current address: Jet Propulsion Laboratory, California Institute of Technology, Mail Stop 169-327, Pasadena, CA 91109, U.S.A.

higher redshifts. In the rest-frame UV, this alignment is even more pronounced, and it occurs in most of  $z \gtrsim 0.7$  powerful radio galaxies (*e.g.* Chambers, Miley, & van Breugel 1987). A variety of physical mechanisms has been proposed to explain the nature of this alignment effect. They include (i) star-formation induced by shocks associated with the radio jet propagation outward from the central AGN (*e.g.* Dey et al. 1997; Bicknell et al. 2000), (ii) scattering of light from an obscured nucleus by dust or electrons (*e.g.* Cimatti et al. 1993; Vernet et al. 2001), and (iii) nebular continuum emission from warm line emitting clouds (*e.g.* Dickson et al. 1995). High-resolution optical and near-IR *HST* observations of HzRGs indicate that the aligned light is probably a mixture of these proposed components (Pentericci et al. 1999, 2001; Stern & Spinrad 1999).

To examine the influence of radio sources on the galaxy formation process, it is important to obtain a large sample of HzRGs, covering a range in redshift and radio power. Despite several intensive search campaigns during the last two decades (see Table 1), the number of known HzRGs is still quite limited: at present only 26 radio galaxies are known with  $z > 3$ . Furthermore, because many of the HzRGs, at least at  $z < 3$ , were discovered from flux limited radio samples, there is a strong dependence of radio power on redshift in the samples of known HzRGs. We therefore constructed a new sample whose aims are (i) to substantially increase the sample of known  $z > 3$  HzRGs, and (ii) to obtain a significant number of  $2 < z < 3$  radio galaxies with radio powers an order of magnitude less than the bright samples. We therefore constructed a sample of ultra steep spectrum (USS,  $\alpha < -1.30$ ;  $S \propto \nu^\alpha$ ) radio sources drawn from new radio surveys that reach flux density levels more than an order of magnitude fainter than previous surveys. USS sources have been successfully used for over two decades to find HzRGs (*e.g.* Röttgering et al. 1994; Chambers et al. 1996; Jarvis et al. 2001a). This technique mainly makes use of a radio  $k$ -correction effect: at higher redshift, an increasingly steeper part of the generally concave radio spectrum shifts to the fixed observing frequencies of the large radio surveys.

This paper is the second in a series of three describing the observations of our sample of 669 USS sources. In Paper I (De Breuck et al. 2000a), we defined our sample. We also presented VLA and ATCA radio images of 410 sources, which provide radio morphological information and the accurate positions needed to identify the optical and/or near-IR counterparts. In this paper, we present the optical and/or near-IR imaging of a sub-sample of 128 sources. We shall use the near-IR magnitudes to obtain redshift estimates based on the Hubble  $K - z$  diagram. In Paper III (De Breuck et al. 2001), we present optical spectroscopy of 46 sources from this imaged sub-sample, including 34 sources with spectroscopic redshifts.

The layout of this paper is as follows. In §2, we describe the optical and near-IR observations and data reduction, paying special attention to the astrometry. We present the results, discuss the morphologies of the near-IR identifications and examine the correlations between the various parameters in §3. In §4, we concentrate on the Hubble  $K - z$  diagram. We discuss the expected redshift distribution

from our sample in §5. We present our conclusions in §6. Throughout, we assume  $H_0 = 65 \text{ km s}^{-1} \text{ Mpc}^{-1}$ ,  $\Omega_M = 0.3$ , and  $\Omega_\Lambda = 0$ .

## 2. OBSERVATIONS AND DATA REDUCTION

We obtained the optical and near-IR images described in this paper at five different observatories between 1996 April and 2000 January. Table 2 gives an overview of the 21 successful imaging observing sessions. We use a consecutive numbering scheme for each session in the project, counting also the sessions where we did not obtain any data, or only spectroscopic data (see Paper III). Table 3 gives a journal of the observations, and Table 4 gives an overview of the instrumental setups.

### 2.1. Target selection

We selected all our targets from the USS sample in paper I. Although we selected the objects at each individual session on the basis of the accessible right ascension range, we have tried to distribute the objects over a large range of spectral index, radio morphology, and 1.4 GHz flux density. The most important improvement of our sample with respect to other recent surveys is the lower flux density limit: the median flux density of our faintest sample (WN) is almost an order of magnitude below all other efforts (Table 1). We therefore selected half of the objects observed in  $K$ -band with the additional criterion  $S_{1400} < 50 \text{ mJy}$ . Although this paper presents only the first batch of images ( $\sim 13\%$  of the sample in  $R$  and  $K$ ), we expect it to be fairly representative for the sample as a whole.

### 2.2. Optical Imaging

#### 2.2.1. Observations

**Lick 3m** We used the Kast imaging spectrograph (Miller & Stone 1994) at the Lick Observatory Shane 3m telescope on Mount Hamilton to obtain images in the “Spinrad night-sky” filter. This yields red magnitudes in the  $r_S$  system, which has an effective wavelength of 6890 Å, and an equivalent width of 1370 Å; the  $r_S$  magnitudes can be related to commonly used photometric systems as determined by Djorgovski (1985)<sup>9</sup>. The field of view of Kast is  $\sim 145''$  square, but there is substantial circular vignetting in all corners. To enlarge the field of view and reduce the chance that the object falls on a bad pixel on the CCD, we dithered the individual exposures by  $\sim 15''$ . We limited the exposure times of the individual exposures to 3–5 minutes to avoid extensive saturation of bright stars in the field.

**ESO 3.6m** To identify the radio source for spectroscopic observations, we took 10–15 minute images with the ESO faint object spectrograph and camera (EFOSC1; Savaglio, Benetti, & Pasquini 1997) on the ESO 3.6m telescope at La Silla. If an object was not detected in 15 min, we did not attempt to obtain a spectrum. We re-observed a large number of these optical “blank fields” in  $K$ -band at Keck observatory (see §2.3.1).

<sup>9</sup> The transformation from Spinrad night-sky  $r_s$  into Johnson  $V R$  is  $(r_s - R) = -0.004 - 0.072(V - R) + 0.073(V - R)^2$ .

**WHT** On two occasions, we used the prime focus imaging platform (PFIP; Carter & Bridges 1995) at the William Herschel Telescope at La Palma to obtain deep  $R$ -band images of USS sources. During the 1997 May run, we used the LORAL CCD, while during the 1999 May run, we used the EEV12 CCD. This resulted in slightly different pixel scales and fields of view (see Table 4).

**Keck** We obtained  $I$ -band images of 3 USS sources with the Low Resolution Imaging Spectrometer (LRIS; Oke et al. 1995) on the Keck II telescope on Mauna Kea. The main use of these deep images was to determine accurate positions and offsets from nearby brighter stars ( $I \lesssim 18$ ) to set up the spectroscopic observations during the same observing session.

### 2.2.2. Data Reduction

For all the imaging data, we performed standard data reductions consisting of overscan bias correction, and flat fielding using a median sky flat, constructed for each individual night from the non-saturated science exposures.

To correct for the circular edges of the Lick images before registering them, we constructed a filter image from the flat-field frame, filtering out all pixels at  $\lesssim 96\%$  of the median central flat-field value. Failure to do so would lead to a strongly increased noise pattern in the outer regions of the registered image. To register the dithered Lick images, we first determined the relative position-shifts between the images using the task `registar` from the IRAF DIMSUM<sup>10</sup> package. Finally, we combined all individual image frames using integer pixels shifts. This is possible, because the PSF is over-sampled by a factor of 2 to 3 (depending on seeing). The use of fractional pixel shifts would require re-sampling of each individual image, which would smear out the PSF in the combined image.

The astrometric calibration and identification of the host galaxy is described in §2.2.3.

We flux calibrated the images using observations from several standard stars obtained during the same night. After including the zero-point, aperture centering and sky background fitting uncertainties given by the `phot` routine, we estimate the photometric uncertainty to be  $\sim 0.2$  magnitudes. We used the IRAF task `phot` to determine fixed aperture magnitudes. We used a  $4''$  diameter aperture for the optical images, because the seeing was often not sufficiently good to justify using a smaller aperture. For images obtained under non-photometric conditions, we used a value of the photometric zero-point determined from previous observations; these magnitudes (indicated with † in Table 6) should be considered as indicative only.

## 2.3. Near-IR Imaging

### 2.3.1. Observations

We used near-IR cameras at the Keck and CTIO observatories to observe sources in both the northern and southern hemispheres. At each observatory, we employed a non-redundant 16-point dithering pattern. The integration times and specific  $K$ -band filter ( $K$ ,  $K_S$  or  $K'$ ) were adapted to the expected magnitudes and sky condi-

tions. We first describe the site-specific details, and next describe the data reduction procedure.

**Keck** The objects that remained undetected after optical imaging ( $R \gtrsim 24$ ) constitute excellent candidates for the highest redshift radio galaxies. We observed these objects with the near-infrared camera (NIRC; Matthews et al. 1994) on the Keck I telescope on Mauna Kea. NIRC contains a  $256 \times 256$  InSb array with a pixel scale of  $0''.151$  pixel<sup>-1</sup>. Depending upon the sky conditions (as measured from the sky counts during the observations), we used either a standard  $K$ , a  $K_S$  or a  $K'$  filter. We used typical integration times of 60 s per pointing, comprised of 3 co-added 20 s frames, in a 16-point non-redundant dithering pattern. Where possible, we reduced the images of the first 16-point cycle during the integration on the next cycle. If the object was clearly detected in one cycle, we did not start a third cycle, in order to save observing time for other sources.

The NIRC requires a  $R \lesssim 18$  guide star to be placed in an offset guider. To achieve this, we often needed to rotate the target field. In some cases, we also had to shift the field by several arcseconds in order to place the guide star on the guider camera. As a result, the images obtained have to be rotated back to orient them in the standard North up, East left orientation, and the objects are not always perfectly centered in the registered frames. Bright stars in the frames display electronic 'bleed trails', for which we do not attempt to correct in the final images.

The data from the 1999 September observing session (K12) were severely affected by instrumental problems due to accidental external illumination of one corner of the detector. This decreased the gain down to  $<10\%$  of the normal value over more than a third of the detector array. During this session, we adapted our dithering pattern such as to avoid placing the identification in this affected areas. These areas are clearly visible in the finding charts shown in the Appendix. The measured counts of the objects in the relevant corners are severely attenuated by this problem, a factor that should be taken into account if the resulting images are being used as finding charts.

**CTIO** For the southernmost sources from our USS sample, we used the CIRIM camera with the tip-tilt system on the CTIO Blanco 4m telescope at Cerro Tololo in the  $f/14$  focal ratio. The detector is a  $256 \times 256$  HgCdTe NICMOS 3 array. We used typical integration times of 120 s per pointing, comprised of 6 co-averaged 20 s frames, in a 16-point non-redundant dithering pattern. To improve the resolution in the images, we performed a tip-tilt correction, using a  $V < 16$  reference star within  $2''.5$  of the radio galaxy.

### 2.3.2. Data Reduction

We reduced the near-IR data using the NOAO IRAF package. After bias subtraction and flat-fielding, we sky-subtracted, registered, and summed the data using the DIMSUM near-IR data reduction package. For most images observed with excellent seeing ( $\lesssim 0''.5$ ), we block-

<sup>10</sup> DIMSUM is the Deep Infrared Mosaicing Software package, developed by P. Eisenhardt, M. Dickinson, A. Stanford, and J. Ward, which is available as a contributed package in IRAF.

replicated the pixels by a factor of 2 before summing the individual images.

### 2.3.3. Astrometry

The mean density of objects down to  $R = 25$  from faint galaxy counts is  $\sim 10^5 \text{ deg}^{-1} \text{ mag}^{-1}$  (Smail et al. 1995). This agrees well with the space density of  $R \lesssim 24.75$  objects in the field of USS radio sources found by Röttgering et al. (1995). Because the optical images reach similar or deeper limiting magnitudes, we can statistically expect to find an unrelated source within  $\sim 11''$  from the radio position. This can lead to a number of possible mis-identifications in cases where the unrelated serendipitous source falls within  $\lesssim 2''$  from the radio position. One way to limit the number of mis-identifications is to use more accurate astrometry. The accuracy of an astrometric solution is dominated by 2 factors: (i) the positional uncertainty of the astrometric reference catalog with respect to the International Celestial Reference Frame (ICRF), and (ii) the accuracy of the transformation of this astrometrical information to the images. The uncertainty in the transformation is mainly influenced by the number of objects available to solve the astrometric parameters (positional zero-points in the x- and y-directions, pixel scales, and rotation) using the positions from the astrometric reference catalog. Because the field of view of the images is generally only a few square arcminutes and we are mainly interested in the central  $\sim \text{arcmin}^2$ , we did not attempt to determine the field distortion parameters.

The uncertainties of the VLA positions with respect to the ICRF are  $\lesssim 0''.2$ . As we will show below, this is 2 to 3 times smaller than the uncertainty between the optical astrometry and the ICRF. In the following, therefore, we will consider only the uncertainties in the optical images. Note that this does not include the uncertainty in the predicted position of the optical/near-IR identification with respect to the radio morphology. In cases where the radio source consists of different components it is possible that the identification does not fall at the midpoint of the radio lobes, but closer to one of the lobes (see *e.g.* De Breuck et al. 1999). In those cases, a visual inspection of the radio source overlaid on the optical/near-IR image often provided an unambiguous identification.

For the optical and near-IR images obtained prior to 1998, we used the astrometric solution from the digitized sky survey (DSS-I). Véron-Cetty & Véron (1996) compared accurate absolute VLBI positions of 153 QSO's with positions from the DSS-I, and found the rms uncertainty of the DSS-I astrometry is  $\sim 0''.6$  in both coordinates over the whole sky. In 1998, the more accurate USNO-A2.0 catalog was published (Monet et al. 1998), which is based on astrometry from the Tycho catalog (Perryman & ESA 1997), generated from the Hipparcos mission. The astrometric uncertainty of this catalog with respect to the ICRF is more than 2 times better:  $1\sigma \approx 0''.25$  (Deutsch 1999). Provided that a good transformation of this astrometry to the object frames is possible, we can identify the radio source to within one seeing element in the optical and near-IR images.

To perform the astrometric calibration on the images, we used the task *XTRAN* in the NRAO *AIPS* package. In almost all cases, the optical images were obtained before

the near-IR image, so we can use the larger field of view of the optical images (see Table 4) to identify the field with the DSS images.

For the astrometric calibration, we only consider stellar objects in the field, because the inclusion of resolved galaxies would introduce additional uncertainties to our solution. In some cases, we had to remove some of the reference objects from our solution in order to get a better fit; these objects are most likely stars with a significant proper motion. The mean number of available reference stars in the optical images is 8 (median is 7). Table 4 lists the mean pixel scales and their  $1\sigma$  deviations, as derived from the *XTRAN* solutions. We find that the uncertainties in the optical pixel scales are generally  $\lesssim 0''.001/\text{pixel}$ , with the largest uncertainties occurring in the images with the smallest field of view, viz. those obtained with Kast at Lick.

In frames where less than 4 reference stars were available, instead of following the above procedure, we used the position of a single star as the origin of the coordinate system, and adopted the pixel scale quoted in Table 4. When a second or third reference star was available, we selected the object that provided the most consistent results, or the object that was closest to the image center.

Because the field of view of the registered *K*-band images barely exceeds  $1' \times 1'$ , we rarely have sufficient stars from the DSS-I, DSS-II or the USNO-A2.0 catalog to perform the same astrometric calibration as in the optical images. We therefore translated the astrometry from the optical images, using stellar objects to  $R \lesssim 24$  in common between the optical and near-IR frames. On average, we used 7 common objects to solve the astrometry in the NIRC images. For the *K*-band images obtained at CTIO, no optical images deeper than  $R \sim 20$  were available, and the uncertainties are significantly larger. Nevertheless 6 radio galaxy identifications determined using this astrometry have been shown to be genuine, as they were all successfully detected spectroscopically with the VLT (see Paper III).

For 4 objects having *K*-band images, but lacking large field of view optical images to find reference objects, we obtained *J*- and *K*-band images using the Gemini twin-arrays infrared camera (McLean et al. 1993) at the Lick 3m telescope. In addition, R. Gal kindly obtained wide field *r*-band images of 3 additional objects (TN J2008–1344, TN J2028–1934, WN J2221+3800) with the Palomar 60'' telescope. We translated the astrometric solution obtained with these shallow wide-field images to align the deeper, but smaller *K*-band images.

Using the astrometric solutions, we could find unambiguous identifications within  $\lesssim 1''$  of the radio positions in  $>90\%$  of the optical images, and  $>94\%$  of the near-IR images (considering only the images with a possible identification within  $8''$  from the radio position). In cases where there was another object within  $\lesssim 2''$ , we adopted as the real identification the object that was closest to the line connecting both radio lobes, or the object with the more diffuse morphology (assuming the other unresolved object to be a foreground star).

### 2.3.4. Photometry

We calibrated the photometry using short observations of standard stars from the UKIRT faint standard list (Casali & Hawarden 1992) or from the list of Persson et al. (1998). For NIRC, this procedure yielded typical zeropoints of  $K_0 = 25.12 \pm 0.03$ ,  $K_{S0} = 24.75 \pm 0.03$ , and  $K'_0 = 25.12 \pm 0.03$  (for 1 count/second, integrated over the source). For CIRIM at the CTIO 4m, we found  $K_0 = 21.73 \pm 0.05$ . We estimated the uncertainties from the variation of the zeropoints determined from different standards during the same night. The zero-points include the airmass term, but we did not correct for airmass variations between the targets, because we observed all of our objects with airmasses  $< 1.7$  (mean airmass 1.15), and the airmass dependence in  $K$ -band is small compared to the aperture centering and sky fitting uncertainties described below.

Because in most cases the redshift was not known at the time of the near-IR observations, we could not predict the expected  $K$ -band magnitudes, as determined from the Hubble  $K-z$  diagram (§4). Consequently, there is a significant range in signal to noise (S/N) in the fixed apertures of the final images, with some of the brighter images reaching S/N levels well over 50, while the faintest detections are only detected down to the  $5\sigma$  level. As a result, the use of isophotal magnitudes is inappropriate. To determine a standard fixed aperture, we first measured the magnitude in a variety of different apertures, with diameters ranging from  $0''.4$  to  $8''$ , using the IRAF task `phot`. Figure 1 shows the resulting variation of the aperture magnitudes as a function of the aperture diameter. It is clear that for the large majority of sources, most of the flux is contained within a  $2''$  diameter aperture. This is also visible from the images (Fig. 2).

Table 7 therefore lists magnitudes in 3 different apertures: (i) a  $2''$  aperture, which, as shown above, corresponds best to the actual size of most galaxies, (ii) a  $4''$  aperture for comparison with the optical magnitudes in Table 6, and (iii) an  $8''$  aperture for comparison with previously published  $K$ -band photometry in the literature (*e.g.* Eales et al. 1997, vB98). The uncertainties quoted are our best estimates, which include both the zero-point uncertainty and the aperture centering and sky fitting uncertainties given by the `phot` routine.

We did not correct the magnitudes for Galactic extinction, but list the expected extinction in the  $K$ -band in Table 7. We obtained these values using the NASA Extragalactic Database (NED), which are based on the  $E(B-V)$  values from the extinction maps of Schlegel, Finkbeiner, & Davis (1998), and converted to  $A(K)$  using the extinction curve of Cardelli, Clayton, & Mathis (1989), under the assumption of  $R_V = A(V)/E(B-V) = 3.1$ . The  $A(K)$  corrections (listed in Table 7) are generally negligible compared to the uncertainties, except in a few objects which lie close to the Galactic plane.

### 3. RESULTS

Figure 2 shows  $8'' \times 8''$  images of the  $K$ -band images, centered on the derived identifications (*i.e.* not the predicted radio position). The grey scale is from  $\mu - \sigma$  to  $\mu + 4\sigma$ , where  $\mu$  and  $\sigma$  are the mean and rms, as determined from a histogram of the sky-subtracted background counts, determined in a source-free region with the

*AZPS* task `IMEAN`. We show  $90'' \times 90''$  finding charts in the Appendix. We show only one finding chart per object, selecting the near-IR image where available, because it is of higher quality than the optical images. All images are shown in the usual orientation with North up and East to the left. Note that this required a generally non-orthogonal rotation of the NIRC images because they were obtained in a orientation that positions a guide star in the offset guider camera (see §2.3.1). We shall now discuss the optical and/or near-IR identification of a number of individual sources, and then consider the magnitude distribution of the sample as a whole.  $K$ -band observations of 2 sources (WN J0117+3715 and WN J1843+5932) from our USS sample have been reported by Villani & di Serego Alighieri (1999).

#### 3.1. Notes on individual sources

**WN J0034+4142:** Although the near-IR identification does not lie at the midpoint, it falls on the line connecting both radio lobes.

**WN J0117+3715:** Villani & di Serego Alighieri (1999) report  $K = 18.20 \pm 0.57$  in a  $3''.88$  diameter aperture for this source, which is consistent with our value ( $K = 17.57 \pm 0.04$  in a  $4''$  diameter aperture).

**MP J0130-8352:** No scale size could be estimated for this source because there is no appropriate PSF-star in the CTIO image.

**MP J0202-5425:** There is a bright stellar object  $\sim 3''$  to the north-east of the near-IR identification, which contaminates the aperture photometry, and the determination of the spatial profile of this source.

**TN J0205+2242:** This galaxy has been spectroscopically confirmed at  $z = 3.506$ . The near-IR surface brightness profile appears very steep for an object at such a redshift, and resembles that of a radio galaxies at  $z < 3$ .

**TN J0218+0844:** The most likely optical identification is the source slightly north of the predicted radio position, although we cannot exclude the source at  $\alpha_{J2000} = 2^h 18^m 25^s.57$ ,  $\delta_{J2000} = 08^\circ 44' 27''.7$ . Because we did not observe this source in  $K$ -band, we do not show a cutout image of this source in Fig. 2.

**MP J0249-4145:** No sources are detected down to  $K \sim 19$  within the positional uncertainty of our ATCA radio map.

**WN J0305+3525:** The near-IR identification is an very diffuse source without a central core component.

**WN J0346+3039:** The near-IR photometry and morphology for this object is highly uncertain due to the problems with the detector during this run.

**WN J0359+3000:** The near-IR identification is uncertain because the radio position is based on the NVSS position only (which has an rms position uncertainty of  $\sim 1''.5$  for this source; Condon et al. 1998). The near-IR photometry and morphology is also highly uncertain due to the problems with the detector during this run.

**MP J0449-5449:** No scale size could be estimated for this source because there is no appropriate PSF-star in the CTIO image.

**WN J0617+5012:** The very faint  $K$ -band identification coincides with the southern radio lobe of a  $z = 3.153$  radio galaxy (see Paper III).

**WN J0741+5611:** Our radio map is of insufficient depth to identify any of the features observed in the field of the  $K$ -band image. We therefore do not show a cutout image of this source in Fig. 2.

**TN J0856-1510:** Our radio map is of insufficient depth to determine the exact optical or near-IR identification. There are 2 candidate identifications in the  $K$ -band image, one at  $\alpha_{J2000} = 08^h56^m12^s.40$ ,  $\delta_{J2000} = -15^\circ10'40''.4$ , and one at  $\alpha_{J2000} = 08^h56^m12^s.37$ ,  $\delta_{J2000} = -15^\circ10'32''.7$ . We therefore do not show a cutout image of this source in Fig. 2.

**TN J0924-2201:** This is the radio galaxy with highest known redshift ( $z = 5.19$ ; van Breugel et al. 1999).

**TN J0936-2243:** The central component and the companion object  $\sim 4''$  to the north both have  $z = 1.479$ . This source is discussed in detail in Paper III.

**WN J1015+3038:** The 3 companion objects may well be part of the same physical source, which is probably at  $z = 0.54$  (see Paper III). If this is the correct, this is object is more than a magnitude redder in  $R-K$  than the other radio galaxies at these redshifts (Fig. 10).

**TN J1033-1339:** No scale size could be estimated for this source because there is no appropriate PSF-star in the NIRC image.

**TN J1049-1258:** The string of objects is aligned with the radio source, which also consists of multiple knots.

**WN J1053+5424:** The near-IR identification is a very diffuse source without a central core component, even though the radio source is a small  $1''.1$  double (see paper I).

**WN J1123+3141:** The near-IR identification of this large radio source (largest angular size  $25''.8$ ) at  $z = 3.217$  is a spectacular interacting system showing extended tidal tails. The  $K$ -band magnitude is  $\sim 2$  magnitudes brighter than the main trend (Fig. 7).

**WN J1314+3649:** This is one of our faintest  $K$ -band identifications. We attempted optical spectroscopy with LRIS at Keck, but did not detect the object (see Paper III).

**TN J1338-1942:** The near-IR identification, a radio galaxy at  $z = 4.11$ , corresponds to the brightest component of a very asymmetric radio source. This source is described in detail by De Breuck et al. (1999).

**WN J1355+3848:** No scale size could be estimated for this source because there is no appropriate PSF-star in the NIRC image.

**TN J1428+2425:** This is a rare  $K$ -band “blank field”. Although our astrometry is based on only 2 stars in common with an image taken with the Gemini camera at Lick observatory, there are no candidate identifications within  $8''$ . We therefore do not show a cutout image of this source in Fig. 2.

**WN J1525+3010:** There appears to be a diffuse halo around the  $K$ -band identification. We have obtained a  $t_{int} = 5400$  s spectrum with LRIS at Keck, but did not detect any optical emission from this source (see Paper III).

**WN J1550+3830:** No scale size could be estimated for this source because there is no appropriate PSF-star in the NIRC image.

**WN J1604+5505:** The near-IR identification is a very diffuse source without a central core component.

**WN J1731+4654:** This is a rare  $K$ -band “blank field”. We obtained the astrometric solution by transfer-

ring a single star from the Lick image and assuming the pixel scale; comparison with 2 other stars common with the Lick image suggests this solution is accurate up to  $\sim 1''$ . There is a source  $5''$  north of the predicted position at  $\alpha_{J2000} = 17^h31^m59^s.68$ ,  $\delta_{J2000} = 46^\circ54'05''.5$ , but this falls well outside the position uncertainty from the FIRST survey. We therefore do not show a cutout image of this source in Fig. 2.

**WN J1836+5210:** The optical and near-IR identifications are ambiguous between a red northern component, and a blue southern component. Table 5 lists the position of the red, northern component, which is slightly closer to the predicted radio position, although both sources might well be part of the same physical system.

**WN J1843+5932:** Villani & di Serego Alighieri (1999) detected this source with  $K = 17.96 \pm 0.19$  in a  $3''.28$  aperture. We did not re-observe it, and refer to their paper for a finding chart.

**TN J2009-3040:** This source has a strong unresolved component, probably a direct contribution from the AGN.

**TN J1941-1952:** The unresolved object  $1''$  west of the near-IR identification is probably a foreground star, and contaminates the aperture photometry.

**WN J2044+7044:** This object appears compact in the  $K$ -band image. We attempted optical spectroscopy with LRIS at Keck, but did not detect any optical emission from the object (see Paper III).

**WN J2213+3411:** The near-IR identification is uncertain, because we lack a high resolution VLA map of this field. However, the NVSS map shows a source that is elongated in the same direction as the proposed identification ( $52'' \times 19''$  at position angle  $-31^\circ$ ).

**WN J2313+4253:** This is the pulsar PSR J2313+4253 (Kaplan et al. 1998; Han & Tian 1999).

### 3.2. Magnitude and color distributions

We identified approximately half of the 83 optically imaged USS sources, while in the near-IR, we found counterparts for  $>94\%$  of the 86 sources observed. Of the 4  $K$ -band non-detections, MP J0249-4145 was obtained with CIRIM at CTIO, and might well have been detected if observed down to fainter levels comparable to the Keck data. Another non-detection, WN J0741+5611, requires more sensitive radio map to determine the possible identification. The remaining 2 sources, TN J1428+2425 and WN J1731+4654, have good radio maps (see paper I), and could be galaxies with extremely faint  $K$ -band identifications or Galactic pulsars.

It is clear that even a moderately deep ( $K \lesssim 20$ ) near-IR survey of radio sources with a 4m class telescope is much more efficient in detecting the galaxy counterparts than deep ( $R \lesssim 25$ ) optical imaging. Once identified, the offsets from brighter stars in the field of the radio galaxy allow one to accurately position the slit for spectroscopic redshift determinations. Moreover, the  $K$ -band magnitude provides an estimate of the expected redshift of the radio galaxy by means of the Hubble  $K-z$  diagram (§4).

Because the magnitude limits of our optical imaging vary from  $R \sim 23$  to  $R \sim 26$ , and half of the observed USS sources are not detected, we cannot construct a reliable optical magnitude distribution. Only one third of the sources are brighter than  $R = 24$ , suggesting that the mean optical

magnitude is probably  $R \sim 25$ . This is significantly fainter than that of the USS sample of Röttgering et al. (1995), who found that the  $R$ -band magnitude distribution in their sample peaks between  $R = 22$  and  $R = 23$ , with 70% of the radio sources identified at  $R < 24$ . This discrepancy is due to 2 main differences between the samples. First, the flatter radio spectral index cutoff ( $\alpha \sim -1.2$ ) in their sample, which selects lower redshift objects than our optically observed sample, with a mean (and median) spectral index of  $\bar{\alpha} \simeq -1.38$ . Second, their sample contains sources with radio flux densities an order of magnitude brighter than our sample.

Our optical magnitude distribution more resembles that of the sample of fainter USS sources by Wieringa & Katgert (1992), who find that half of their sources have  $R > 24$ . The Wieringa & Katgert (1992) sample has a similar spectral index selection ( $\alpha_{327}^{608} < -1.1$ ) as the Röttgering et al. (1995) sample, but has flux densities comparable to our WN sample. This suggests that the lower radio flux densities may explain the fainter optical magnitudes, because the host galaxy absolute magnitude appears to be correlated with radio luminosity (*e.g.* Best, Longair, & Röttgering 1998; Lacy, Bunker, & Ridgway 2000). Such a correlation could arise if the host galaxies of the more powerful radio sources contain a greater mass of stars, and assuming that their central black holes accrete at near-Eddington rates. We return to this point in §4.2.

Figure 3 shows the distribution of  $K$  magnitudes. The mean/median  $K$ -band magnitude is  $K = 19.26/19.19$  in a  $2''$  diameter aperture ( $K = 18.57/18.72$  in a  $4''$  aperture). The distribution appears to be slightly asymmetric, in the sense that the tail of sources with magnitudes fainter than the mean seems to be broader than the bright-end tail, which cuts off at  $K = 17.5$ . This may be partially due to our prior selection of objects undetected on the POSS ( $R \lesssim 20$ ).

We can get an idea of the content of the sources in our sample from the  $R - K$  color distribution shown in Figure 4. This histogram consists of only 37 sources, of which 27 are non-detections in the  $R$ -band. This is mostly due to the nature of our observational program, where we assigned lower priorities in our  $K$ -band imaging campaign to those objects that had been previously detected in the  $R$ -band. From this histogram we can conclude that at least half of the sources observed have  $R - K > 4$ , at least a third have  $R - K > 5$ , and at least 10% are bona fide extremely red objects (EROs; *e.g.* Elston, Rieke, & Rieke 1988; Graham & Dey 1996). Note that due to the shallowness of the optical imaging, these are mostly lower limits. We discuss the  $R - K$  color evolution in §4.3.2.

### 3.3. Morphology

To obtain basic morphological information of the host galaxies (ellipticity and position angle), we used the IRAF-STSDAS task `ellipse` to fit surface brightness profiles in the near-IR images. The profiles are generated by fitting elliptical isophotes to the data, with the center, ellipticity, and position angle of each ellipse allowed to vary. The iterative method used in the fitting of each ellipse is described in Jedrzejewski (1987). We fit each source interactively, and continued fitting out-

ward isophotes until the ellipticity or position angle started showing large variations or nearby companions were picked up. We did not attempt to fit radial profiles for (i) sources observed with CIRIM at CTIO, because the seeing was too poor, (ii) sources with companion objects within  $< 2''$ , (iii) sources fainter than  $K \sim 20$  in a  $2''$  diameter aperture, and (iv) sources with an obvious non-elliptical morphology (*e.g.* TN J1049–1258 and WN J1123+3141). Excluding these sources, we retain 44 objects. Table 7 lists their ellipticities and position angles.

A visual inspection of Figure 2 shows the generally compact structure of the  $K$ -band identifications, even with the good seeing of the Keck images. This is partly due to our observing strategy which cut short the integration times of objects that could be detected in quick mountain reductions of the first frames. Consequently, we did not obtain images with a high signal/noise ratio out to large distances. This is illustrated by the fact that more than half of the flux of the  $8''$  diameter apertures is enclosed within a  $2''$  aperture (See also Fig. 1). This makes it impossible to determine surface brightness profiles out to sufficiently large radii to differentiate between standard galaxy functional forms such as de Vaucouleurs or power-law disc models.

However, it is possible to estimate the half light radii of the host galaxies, using a procedure described by Lacy, Bunker, & Ridgway (2000). This method assumes that the host galaxies have de Vaucouleurs profiles (Roche, Eales & Rawlings 1998, note that disc models do not give significantly different best-fitting half light radii). To estimate the half light radius in an image, we constructed a set of model galaxies with circular de Vaucouleurs profiles with a range of half light radii. We then convolved these model galaxies with a PSF profile from a nearby star, and normalized them to match the total flux of the observed galaxy. We subsequently subtracted the model galaxies from the data and measured the rms in the residual image. Finally, we fitted a second-order polynomial to the three model galaxies yielding the lowest rms residuals, and determined the half light radius from the minimum of this polynomial.

The derived values need to be corrected for ellipticity. To correct for this, we did not use the ellipticities quoted in Table 7, because the values are derived from the outer isophote only, which may be subject to large uncertainties due to the inclusion of unresolved companion objects. Instead, we assumed a mean ellipticity of  $e = 0.2$ , following Lacy, Bunker, & Ridgway (2000). Table 7 lists the corrected estimates of the half light radii for 36 galaxies where this procedure was successful. The other objects either have no star in the field that can be used as a PSF, have too low signal/noise, or obvious non-elliptical morphologies due to strong interactions with the radio source or companion objects.

The median  $r_{hlr}$  is  $0''.48$  (mean is  $0''.60$ ). This is similar to the values measured by Roche, Eales & Rawlings (1998) for a sample of 6C galaxies at  $z \sim 1$  (mean  $0''.55$ , median  $0''.48$ ). However, our values are slightly smaller than those found by Lacy, Bunker, & Ridgway (2000) for a sample of 7C sources (mean  $1''.24$ , median  $0''.90$ ). These authors argue that the smaller  $r_{hlr}$  in the 6C sample could have been underestimated due to poor seeing, but our sample was observed with better seeing than the 7C, and still finds

smaller  $r_{htr}$ . To examine the dependence of  $r_{htr}$  on intrinsic source parameters, such as redshift or radio power, it will therefore be important to obtain more spectroscopic redshifts for our sample (at present, we only have spectroscopic redshifts of 7 objects with measured  $r_{htr}$ ). We conclude that the present data are insufficient to examine the evolution of the host galaxies of powerful radio sources.

### 3.4. Correlations with source parameters

Because we detected virtually all the sources from our sample we observed in  $K$ -band, we can now examine correlations between the parameters determined from the near-IR images (magnitude, color, ellipticity, position angle) and other source parameters (redshift, radio power, radio spectral index, radio size, radio position angle, emission line luminosity). Paper I and III list the radio and spectroscopic parameters, and how they were determined. Because the vB98 sample consists of well-studied objects, we added their data to our sample to search for possible correlations.

#### 3.4.1. Correlations with redshift

The most obvious correlation is between redshift and  $K$ -band magnitude, the so called Hubble  $K - z$  diagram, which is discussed separately in §4. In §4.3.2, we supplement our sample with data from the literature to study the color evolution of the radio galaxy hosts.

#### 3.4.2. Correlations between morphological parameters

The radio and near-IR morphologies do not show strong correlations, except for the tendency for the main axis of the near-IR identification and the radio position angle to be aligned. We return to this point in §3.5.

#### 3.4.3. Correlations with emission line luminosities

For less than 20 sources we have information on the emission line luminosity of  $\text{Ly}\alpha$  and/or  $\text{C IV } \lambda\lambda 1549$ . Neither these luminosities nor their ratio appear to be correlated with any of the photometric or morphological near-IR parameters, although a weak correlation between these parameters would not be detected in such a small sample.

#### 3.4.4. $K$ -band magnitude and radio spectral index

Because we use both the steepness of the radio spectral index and the faintness of the  $K$ -band magnitude to select the highest redshift radio galaxies, it is of interest to examine if both parameters are correlated through their mutual redshift dependence. In our inhomogeneous sample, the low frequency spectral indices and  $2''$  or  $4''$  diameter aperture  $K$ -band magnitudes are correlated at the 88% significance level. However, we do not consider this number representative because of (i) the limited spectral index coverage  $\alpha < -1.2$  in our sample, (ii) the incomplete  $K$ -band imaging of  $<13\%$  of our sample, and (iii) the radio power dependence within our sample (see §4). To illustrate the importance of this third point, we note that mean/median  $K$ -band magnitude of sources observed from our radio brightest MP sub-sample (see Paper I) is  $\bar{K}_{MP} = 18.6$ , while for our  $\sim 10$  times fainter WN sample,  $\bar{K}_{WN} = 19.4$ . For these same sub-samples, the median spectral indices are  $\bar{\alpha}_{MP} = -1.23$  and  $\bar{\alpha}_{WN} = -1.41$ .

#### 3.4.5. $K$ -band magnitude and radio size

Figure 5 shows the radio size plotted against  $K$ -band magnitude. The faint  $K > 20$  sources are all very small in the radio ( $\lesssim 3''$ ), while the brighter sources have a large range of radio sizes. Because the  $K$ -band imaging has an almost complete identification fraction, and the identifications of the large radio sources are unambiguous, we can exclude that the distribution in Figure 5 is due to selection effects.

The spectroscopic observations (see Paper III) concentrated on these weak sources with small radio sizes. Of the 18  $K > 20$  detections 13 were observed spectroscopically. We could determine the redshift of 7 objects, which have a mean of  $\bar{z} = 3.67$ , range from  $z = 2.54$  to  $z = 5.19$ , and include the 4 highest redshift objects from our sample. For 3 objects, we did not detect any optical emission in our deep ( $t_{int} = 1 - 1.5$  h) Keck spectra, while the remaining 3 objects have a faint optical continuum down to  $4800 \text{ \AA}$ , but no detectable emission or absorption lines. In Paper III, we discuss the possible nature of the objects lacking redshift determination.

Although we obtained redshifts for only 39% of the  $K > 20$  objects with small radio sizes, they are significantly more distant than the other objects in our sample. This suggests that an angular size cutoff of  $\lesssim 5''$  could also be used as an additional filter to select the highest redshift objects, prior to the  $K$ -band imaging. Such a cutoff has been used in several samples designed to find HzRG, such as the 6C\* USS sample of Blundell et al. (1998) and the MG sample of Stern et al. (1999). However, although the largest radio galaxy at  $z > 4$  is  $4''3$  (8C 1435+635; Lacy et al. 1994), 5 out of the 16 known  $3 < z < 4$  radio galaxies are  $>10''$  (De Breuck et al. 2000b), including 4C 41.17 at  $z = 3.8$ , which has a radio size of  $13''$ . It is therefore likely that applying such an angular size cutoff will also exclude a number of  $z > 4$  radio galaxies, and introduce additional selection effects.

### 3.5. Radio-near-IR alignment

Figure 6 shows a histogram of the difference in orientation between the position angle of the radio structure and the orientation of the near-IR image, as determined from the major axis of the outer fitted isophote in the  $K$ -band image (§3.3). There is a clear trend for the radio and *observed*  $K$ -band morphologies to align. This trend is more obvious when we consider only the radio sources larger than  $5''$ , whose radio position angle can be measured more accurately (shaded histogram in Fig. 6). There are at least 2 additional objects in our sample that show an even closer correlation between the radio and near-IR morphologies: TN J1049-1258 and WN J1123+3141 ( $z = 3.217$ ). This can also be seen in Fig. 2, where the radio position angle is indicated atop  $8'' \times 8''$  cutout images of the 81 detected objects.

Our result is consistent with the high-resolution NICMOS  $H$ -band observations of 19 radio galaxies with  $1.68 < z < 3.13$  (Pentericci et al. 2001), which showed radio structures that are often (although with several notable exceptions) aligned with the near-IR morphologies. In contrast, using  $K$ -band images from B2/6C sample, Eales et al. (1997) found no alignment effect, and argued



that such a radio - near-IR alignment effect only occurs in the most luminous radio sources. Because our sample contains sources of similar or lower radio luminosity than the B2/6C sample, Figure 6 leads us to question the significance of the distribution based on only 9 objects shown in Figure 6 of Eales et al. (1997). We believe our result is more robust because (i) our sample is 5 times larger, (ii) the seeing in our observations is superior (and the pixel scale is 3 times smaller), and (iii) our limiting magnitude is  $\sim 2$  magnitudes fainter.

Together with the previous NIRC observations of vB98 and the NICMOS observations of Pentericci et al. (2001), our data provide further evidence for the existence of a radio-near-IR alignment effect. Because our sample contains objects over a wide redshift range, the question of the origin of the observed  $K$ -band emission arises. The spectroscopic redshifts of  $\sim 25\%$  of the objects with  $K$ -band images from our sample indicate that  $\sim 33\%$  are at  $z < 2$ ,  $\sim 33\%$  at  $2 < z < 3$  and  $\sim 33\%$  at  $z > 3$  (paper III). For the objects not yet observed spectroscopically, we estimate redshifts  $1 < z < 3$ , based on the Hubble  $K - z$  diagram (see §4). Therefore, the observed  $K$ -band most likely samples rest-frame  $\sim 5500 \text{ \AA}$  to  $\sim 11000 \text{ \AA}$ . The absence of strongly nucleated morphologies in the  $K$ -band images suggests there is no strong direct contribution from the AGN to the  $K$ -band emission. The images also do not show cone-like morphologies, which may be caused by AGN photo-ionization of regions swept up by the passage of the radio jets, as seen in the  $H\alpha$  image of B3 0731+438 (Motohara et al. 2000). However, for most sources, we cannot exclude a contribution from strong emission lines, which may influence the *observed* near-IR emission in the outer region. In several  $z \sim 1$  radio galaxies with high-resolution *HST* images, the extended emission lines clearly strengthen the alignment effect, but they cannot account for it completely (Longair, Best, & Röttgering 1995). Only spatially resolved spectroscopy can determine the exact contribution from emission lines. Such a contribution can also be excluded if the redshift is in an interval where there are no strong lines in the observed  $K$  or  $K_S$  band. Unfortunately, we have determined redshifts of only 40% of the objects observed (see Table 3). One example where we can exclude a significant emission line contribution is TN J1033-1339 ( $z = 2.425$ ). In objects like these, stellar light seems to be the most likely origin of the  $K$ -band emission.

#### 4. THE HUBBLE $K - z$ DIAGRAM

During the last 2 decades, the Hubble  $K - z$  diagram has played an important role in the search for and the study of high redshift galaxies (*e.g.* Lilly & Longair 1984; Eales et al. 1997, vB98). For example, the first radio galaxy discovered at  $z > 3$  was selected from a radio sample on the basis of a faint  $K \sim 18.5$  magnitude (Lilly 1988). In our sample, we combine this faint  $K$ -band selection with our radio USS criterion.

##### 4.1. The $K - z$ diagram for radio galaxies

Figure 7 presents a  $K - z$  diagram that includes the 22 objects with  $K$ -band data and redshifts, augmented with data of 3 samples drawn from the literature: the 3C sample (Lilly & Longair 1984; Dunlop & Peacock 1993), the 6C/B2 sample (Eales et al. 1997; Rawlings, Eales, & Lacy 2001), and the sample of HzRGs observed with NIRC by vB98. We followed the same photometric procedures as described in Eales et al. (1997) to ensure that all magnitudes are on the same metric system. This involves correcting the magnitudes measured in an  $8''$  diameter aperture to a standard 64 kpc aperture<sup>11</sup>, assuming the emission within an aperture of radius  $r$  is proportional to  $r^{0.35}$ . This aperture correction brightens the magnitudes by 0 – 0.1, depending on redshift. As shown in Figure 1, the  $8''$  diameter aperture is too large for most objects, but no smaller-aperture magnitudes have been published for large samples in the literature.

Our new HzRGs obey the same relation as the previous data, but have a larger scatter than the objects observed by vB98, even though the same observational setup was used in both samples. We now examine the possible reasons for this.

**Contribution from emission lines.** Using near-IR spectroscopy of HzRGs, Eales & Rawlings (1993) argued that emission lines may contribute 0 – 100% to the  $K$ -band magnitude. vB98 avoided this problem by observing their sample using specific  $K$ -band filters which avoid rest-frame wavelengths including strong emission lines. Our observations could be more subject to line contamination because we used only the  $K$ - and  $K_S$ -band, mostly without prior knowledge of the spectroscopic redshift. However, the only lines that are expected to contribute significantly to the  $K$ -band magnitude are [O II]  $\lambda 3727$ , [O III]  $\lambda 5007$ , and  $H\alpha$  (see McCarthy 1993). This would lead to an asymmetric scatter towards brighter magnitudes around  $z \sim 4.9$ , 3.4, and 2.3. For example, Armus et al. (1998a) found that the [O III] lines in 4C +19.71 at  $z = 3.594$  contribute 34% to the  $K$ -band magnitude. However, only one object in our sample shows a clear excess magnitude at these redshifts (WN J1123+3141), but this is an exceptional, complex merging system, in which enhanced star-formation may well contribute more to the  $K$ -band luminosity in the continuum than optical line emission ([O III]  $\lambda 5007$ ). Moreover, because our sample contains less radio powerful sources, the emission lines are also fainter, due to the correlation of emission line luminosity with radio power (Rawlings & Saunders 1991; Jarvis et al. 2001b). We therefore dismiss this possibility.

**Direct contribution from the AGN.** According to unified models, the hosts of radio galaxies harbor hidden AGN which are shielded from our direct view by thick obscuring material, while in quasars there is a direct line of sight toward the unresolved central AGN. Because the AGN emission is extremely bright relative to the emission from the stellar population in the host galaxy, even a small partially obscured contribution could have a significant influence on the total integrated  $K$ -band magnitude.

<sup>11</sup> Eales et al. (1997) used a 63.9 kpc aperture, because the  $8''$  aperture used for most of the  $K$ -band data in the literature supposedly corresponds to this value at  $z = 1.0$  in their adopted cosmology ( $H_0 = 50 \text{ km s}^{-1} \text{ Mpc}^{-1}$ ,  $\Omega_M = 1.0$ , and  $\Omega_\Lambda = 0$ ). In fact,  $8''$  corresponds to 68.1 kpc, but we continue to use 64 kpc for the sake of uniformity in the literature.

However, this contribution would appear unresolved and in §3.3 we found no evidence for such a component in the  $K$ -band images. Although our images are not of sufficient quality to put strong limits on a possible direct AGN contribution, we would have clearly detected cases where this component would dominate the  $K$ -band emission.

The low selection frequency (325 or 365 MHz) of our USS sample also tends to avoid objects which are dominated by a strong flat spectrum radio core (*e.g.* Blundell et al. 1998). Those objects are thought to be more Doppler boosted due to a decrease in the angle between the jet-axis and the line of sight. Such small viewing angles would increase the chance of a direct line of sight towards the central AGN like in quasars.

At  $z \sim 1$ , there is also observational evidence from studies of other samples of radio galaxies that the contribution of AGN emission to the  $K$ -band emission is small. The results of thermal IR observations of 3C and lower redshift radio galaxies by Simpson, Rawlings & Lacy (1999) and Simpson, Ward, & Wall (2000) show that even in the most powerful radio sources, the contribution by AGN emission to the  $K$ -band magnitude is  $\lesssim 10\%$ . Near-IR polarimetry observations by Leyshon & Eales (1998) indicate that scattered quasar light makes only a small contribution at near-IR wavelengths, even in sources where this contribution is important in the UV and optical.

#### 4.2. Relation between radio power and $K$ -band magnitude at given redshifts.

Based on the observation that the  $K$ -band magnitudes of the stellar populations of  $z \sim 1$  3CR radio galaxies are brighter than those of the lower radio power 6C radio galaxies, Best, Longair, & Röttgering (1998) argued that the stellar masses of the more powerful radio galaxies are greater. The most powerful radio sources would possess radio beams with kinetic powers close to the Eddington limiting luminosity of a central super-massive black hole. The recently found correlation between black hole mass and galaxy velocity dispersion in nearby elliptical galaxies suggests a causal connection between the formation and evolution of their central black hole and bulge (Gebhardt et al. 2000). This may also imply that the mass of the black hole scales with the mass of the host galaxy, in which case the most powerful radio sources will contain more massive central engines together with their larger stellar mass. Additional evidence for the existence of such a relation was provided recently by Lacy, Bunker, & Ridgway (2000) who found that the *rest-frame*  $R$ -band magnitudes  $M_R$  of  $z \sim 1$  radio galaxies increase with radio luminosity.

To examine the relation between radio power and  $K$ -band magnitude quantitatively, we first fit a linear relation to the  $\log_{10}(z)$  vs.  $K_{64kpc}$  relation. This line, shown in Figure 7, does not have any direct physical meaning, and only serves to measure the deviation from the main trend at a certain redshift. We determined the radio power at 1.4 GHz rest-frame in a consistent way, using flux densities from the WENSS 325 MHz (Rengelink et al. 1997), Texas 365 MHz (Douglas et al. 1996), and NVSS 1.4 GHz (Condon et al. 1998); see De Breuck et al. (2000b) for more details. This procedure provides radio powers for 99 radio galaxies with known  $K$ -band magnitudes. Figure 8 plots this deviation from the  $K - z$  relation against the ra-

dio power at 1.4 GHz. The statistical significance of this correlation is 99.94%, with a Spearman rank correlation coefficient of  $r = -0.34$ . Considering only the 87 sources at  $z < 2$ , the significance drops to 95%, while for the 12  $z > 2$  sources, the significance drops to 88%. Of course the linear fit to the  $\log_{10}(z)$  vs.  $K_{64kpc}$  relation is a serious over-simplification which may well introduce an artificial dependence in Figure 8. However, fitting a second order polynomial to the  $K - z$  relation has a minor (positive) influence on the significance of the deviation  $K - z/P_{1400}$  relation. We note that the data used to determine this correlation are either from complete samples of radio surveys, or from our sample, and therefore have complete  $K$ -band information. So there is no selection effect against faint  $K$ -band sources. Furthermore, we have concentrated on such fainter  $K$ -band sources in our spectroscopic campaign (paper III).

We conclude that at  $z \sim 1$ , the relation seems to be well established (see also Eales et al. 1997), but a larger sample of less radio powerful  $z > 2$  radio galaxies is needed to confirm the extension to higher redshifts. However, if the relation holds, it could provide an explanation for the higher scatter in our sample, compared to the sample observed by vB98 (both observed with NIRC). Our new USS sample is based on radio surveys that are 10 – 100 times fainter than the ones used to find the other HzRGs (see Fig. 1 of De Breuck et al. 2000b), and therefore includes radio sources with a much larger range of radio luminosities, while the vB98 sample mainly contains radio galaxies with  $P_{1400} > 10^{36}$  erg s $^{-1}$ Hz $^{-1}$ . Because radio power and emission line luminosity in HzRGs are correlated (*e.g.* Rawlings & Saunders 1991; McCarthy 1993; De Breuck et al. 2000b), the emission line luminosities are expected to be weaker in our sample. This could also introduce a spectroscopic bias against less powerful radio sources, as it is harder to determine their redshifts. The  $K$ -radio power relation would then propagate this bias towards brighter  $K$ -band magnitudes. Our sample is less subject to this because we have obtained deep spectra with the Keck telescope, while the vB98 sample was based on previous USS samples which used only 3–4m class telescopes for optical spectroscopy.

The connection between the radio and emission line luminosities is most likely established through a mutual dependence on the black hole mass. This can also explain the small range in  $K$ -band magnitudes through the dependence of the host galaxy stellar mass on the same black hole mass (Best, Longair, & Röttgering 1998; Lacy, Bunker, & Ridgway 2000). Assuming the radio power – host galaxy mass relation is the main determinant of the trends with radio power in the  $K - z$  diagram, this would argue that the most massive galaxies at the highest redshifts can be found by selecting the most powerful radio sources.

#### 4.3. Comparison with radio-quiet galaxies

##### 4.3.1. $K - z$ diagram

For almost two decades, this tight correlation in the Hubble  $K - z$  diagram has been used as one of the strongest indications that radio galaxies are identified with massive ellipticals at high redshift. However, this argument is based on the extrapolation from the  $z \lesssim 1$  observations,

where this is indeed the case (*e.g.* Lilly & Longair 1984). A direct comparison between the stellar populations of radio-loud and radio-quiet galaxies at  $z \gtrsim 1$  has not been possible until only very recently. This situation has now changed with the availability of extremely deep imaging and spectroscopy of the Hubble Deep Field (HDF-North; Williams et al. 1996).

Dickinson et al. (2001) obtained a  $t_{\text{int}} = 22.9\text{h}$   $K$ -band image of the HDF-North using the IRIM camera at the Kitt Peak National Observatory 4m telescope in 1996 April. These images reach a formal  $5\sigma$  limiting magnitude of  $K = 21.92$  ( $2''$  diameter aperture), which is comparable to or fainter than our NIRC H<sub>2</sub>RG images. M. Dickinson kindly provided us with a list of all 185 objects in the HDF-North with known spectroscopic redshifts, and their  $K$ -band magnitudes or limits. Because the  $K$ -band HDF-North image has much poorer resolution ( $\sim 1''$  seeing) than the space-based *HST* images, the magnitudes of the individual objects were not measured in standard apertures. Instead, only objects detected in the *HST* NICMOS F110W ( $J$ -band) and F160W ( $H$ -band) images (Dickinson 1999) were selected, convolved to match the ground-based  $K$ -band PSF, and then fit to the  $K$ -band data. In this way overlapping objects are deblended, and meaningful fluxes and limits to every object detected in the NICMOS data can be assigned, regardless of whether it can be detected or not in the ground-based  $K$ -band image. These magnitudes can be considered as approximately total magnitudes, and are calibrated to the same Vega-based photometric system, as also used for the observations of the radio-loud galaxies. The 185 spectroscopic redshifts have been compiled by M. Dickinson from identification campaigns of various groups. They are therefore a heterogeneous mix, and do not intend to be complete in any way. The highest redshift galaxy in the sample is HDF 4-473.0 at  $z = 5.60$  (Weyman et al. 1998).

Because of the small survey area, the HDF-North catalog contains few  $z \lesssim 0.3$  galaxies. To increase the number of radio-quiet galaxies at low redshifts ( $z \lesssim 1$ ), we used the redshifts and  $K$ -band magnitudes of the Hawaii survey (Cowie et al. 1994; Songaila et al. 1994). These magnitudes were measured in a  $3''$  or  $3.5''$  diameter circular aperture, and then corrected to total magnitudes using an average correction determined from all bright isolated objects in the field (see Cowie et al. 1994, for details). Songaila et al. (1994) provide spectroscopic redshifts for the  $K < 20$  objects. The highest redshift galaxy in this sample is at  $z = 1.154$ , and the list also contains a  $z = 2.33$  BALQSO (Cowie et al. 1994), which we include for completeness, although it can not be directly compared with the other radio-quiet or radio-loud galaxies.

Because the 64 kpc metric apertures determined for the radio galaxies in Figure 7 are also our best estimate for their total magnitudes, we can now directly compare the  $K$ -band magnitudes of radio-quiet and radio-loud galaxies over the entire redshift range  $0 < z < 5.6$ . Figure 9 shows this composite Hubble  $K-z$  diagram of radio-quiet and radio-loud galaxies. The most obvious difference with Figure 7 is the almost complete absence of a relation in the radio-quiet objects. There also appears to be a deficiency of  $K > 20$  objects at  $z \lesssim 0.3$ , but this is due to the limited survey area of the HDF, and the  $K < 20$  limit of the spec-

troscopy of the Hawaii survey. This is also the most likely explanation for the absence of bright radio-quiet galaxies. Also note the dearth of sources in the 'redshift desert' at  $1.5 \lesssim z \lesssim 2$ , where no bright emission lines are observable with optical spectrographs.

Figure 9 shows that at  $z \lesssim 1$ , the radio-loud galaxies trace the bright envelope of the radio-quiet galaxies, while at  $z \gtrsim 1$ , they are  $\gtrsim 2$  magnitudes brighter. Provided the non-stellar contributions to the  $K$ -band emission are negligible (as argued above), this is some of the strongest evidence to date that powerful radio galaxies pinpoint the most massive systems out to the highest redshifts currently accessible. Although mass estimates are very uncertain, Best, Longair, & Röttgering (1998) estimate masses exceeding  $10^{11}M_{\odot}$  for  $z \sim 1$  3CR radio galaxies. However, this is consistent with other determinations: Dey & Spinrad (1996) derive a kinematically determined mass estimate of  $\sim 8 \times 10^{10}M_{\odot}$  for the central region of the  $z = 0.81$  radio galaxy 3C 265. These values are an order of magnitude smaller than the ones determined for HDF field galaxies: Papovich, Dickinson & Ferguson (2001) derive masses of  $\sim 10^{10}M_{\odot}$  for  $2.0 \lesssim z \lesssim 3.5$  Lyman break galaxies in the HDF-North. This illustrates that the large difference in survey area between the radio and deep optical surveys can allow the detection of such rare massive objects.

#### 4.3.2. $R-K/z$ diagram

The  $R-K/z$  diagram has been widely used to argue that the stellar population in radio galaxies is dominated by an evolved population formed at high redshifts ( $z_{\text{form}} \gtrsim 5$ ). At  $z \gtrsim 1$ , the scatter increases due to the  $k$ -correction effect shifting contributions from younger starbursts into the *observed*  $R$ -band (*e.g.* Dunlop et al. 1989). Especially at the highest redshifts ( $z > 3$ ), there is evidence for the presence of substantial amounts of star-formation (*e.g.* Dey et al. 1997; Papadopoulos et al. 2000). However, these recent starbursts (possibly induced by the radio activity) cannot produce the majority of the stellar population, as this would produce too large a scatter in the  $K-z$  diagram (Rocca-Volmerange & Guiderdoni 1990). An additional explanation for the increased  $R-K$  scatter at  $z \gtrsim 1$  could be the increasing contributions from non-stellar components. This is supported by spectropolarimetry observations suggesting that a scattered quasar component dominates the UV spectra of radio galaxies at  $z \sim 1$  (*e.g.* Tran et al. 1998) and  $z \sim 2.5$  (Vernet et al. 2001).

To examine if our radio galaxies differ in any way from field galaxies, we also compiled the  $R-K$  colors of radio and HDF galaxies. Because our sample contains only 14 spectroscopically confirmed objects with  $R-K$  information, we supplemented our sample with 130 galaxies from the MRC 1Jy survey (McCarthy 1999) and 41 galaxies from the 7CRS (Willott, Rawlings & Blundell 2001b). While all these radio galaxies have spectroscopic redshifts, this does not mean they are an unbiased sample. Willott, Rawlings & Blundell (2001a) have made photometric redshift estimates for the 7 sources in their 7CRS sample which did not yield redshifts after optical spectroscopy, and found that 6 of them have  $R-K > 5.5$ . This is consistent with the results from Keck spectroscopy of our USS sample (De Breuck et al. 2001): of the 5 sources

that did not yield a redshift after  $\sim 1$ h exposures, one has  $R - K = 5.8$ , while the others have limits  $R - K > 4$ .

For the HDF, we use the photometry and photometric redshifts of Fernández-Soto, Lanzetta, & Yahil (1999). To obtain  $R$ -band colors, we interpolated between the mean wavelengths of the F606 (6031 Å) and F801 (8011 Å) filters to 6940 Å. We also include the color evolution predicted from stellar evolution synthesis models, calculated with PEGASE 2 (Fioc & Rocca-Volmerange 1997, 1999). The 5 model grids with  $z_{\text{form}} = 2, 3, 4, 5, 6$  represent an instantaneous burst, using a Salpeter IMF ( $0.1 < M < 120 M_{\odot}$ , solar metallicity, and no infall).

Figure 10 shows the combined  $R - K/z$  diagram of radio and optically selected galaxies. At  $z \lesssim 2$ , the radio galaxies are clearly redder than the field galaxies, and closely follow the predictions from evolved stellar populations. At higher redshifts, the scatter increases, which can be explained by different competing factors, including: (i) the increasing contribution of young stars and non-stellar emission in the  $R$ -band, (ii) the incompleteness of the spectroscopic redshift information which tends to be more significant for the reddest objects (Willott, Rawlings & Blundell 2001a), and (iii) reddening due to dust (Armus et al. 1998a; Archibald et al. 2001; Reuland et al. 2001). Because the amount of dust emission appears to increase with redshift Archibald et al. (2001), it is unlikely that the redder colors at  $z \lesssim 2$  are due to reddening by dust. We therefore conclude that,  $z \lesssim 2$  radio galaxies appear clearly redder than the HDF field galaxies, and interpret this as evidence for the more evolved stage of their stellar populations. At  $z \gtrsim 2$ , a detailed decomposition of the different components contributing to the  $R$ - and  $K$ -band emission would be needed to make a proper comparison between both classes.

Some of the field galaxies have colors similar to those of the radio galaxies, indicating some field galaxies also contain evolved stellar populations, or are very dusty (*e.g.* Armus et al. 1998b; Cimatti et al. 1998; Dey et al. 1999b). The fact that almost no HDF galaxies have colors significantly redder than the radio galaxies supports the idea that the latter formed at higher redshift. However, the larger scatter in  $R - K$  color for the HDF galaxies does not imply that they are not ellipticals, as morphologically selected samples from the HDF have found bluer field ellipticals (*e.g.* Schade et al. 1999; Dickinson 2000).

#### 4.3.3. The fraction of massive galaxies which harbour powerful radio sources

What fraction of massive galaxies at high redshift do powerful radio sources represent? To answer this question, a large-area spectroscopic survey of  $K \sim 20$  galaxies, with follow-up radio observations would be needed. Although the Hawai'i survey covers 250 arcmin<sup>2</sup> for  $K < 16$  objects, this area is limited to 5 arcmin<sup>2</sup> for  $K < 20$  (Songaila et al. 1994), similar to the coverage of the HDF. This is too small to detect statistically significant numbers of galaxies at the highest redshifts.

Nevertheless, it is worth pointing out that the  $z > 4$  galaxy in the HDF with the brightest radio emission ( $S_{1400} = 470 \mu\text{Jy}$ ) is more than a magnitude brighter in  $K$ -band than the other 6 at  $z > 4$  (VLA J123642+621331 at  $z = 4.424$ , Waddington et al. 1999). There is now cir-

cumstantial evidence that this object contains an AGN, including (i) the detection of an unresolved component in a  $0''.026$  resolution radio image obtained with the European VLBI Network (EVN) (Garrett et al. 2001), and (ii) the detection of X-ray emission with *Chandra* which is consistent with the optical to X-ray flux ratio seen in local AGN (Brandt et al. 2001).

At lower redshift, VLA J123644+621133 is a  $z = 1.050$  FR I source (Richards et al. 1998). The  $K = 16.92$  of this object is comparable to the the brightest 3C sources at these redshifts. Several other AGN in the HDF detected in deep radio and/or *Chandra* X-ray maps (Hornschemeier et al. 2000) inhabit fairly normal galaxies. One of the *Chandra* sources with a photometric  $z_{\text{phot}} \simeq 2.6$  is an extremely red object with  $K = 22.07$ , and is likely an obscured AGN (M. Dickinson, private communication). Such obscured AGN at  $z \lesssim 2$  might also be present in our radio selected sample (see paper III).

To summarize, radio galaxies remain the most efficient tracers of the most massive galaxies at the highest redshifts accessible with optical spectrographs. Some of the most luminous objects at a given redshift in the optically selected surveys also appear to harbour an AGN, but the present sample is too small to determine the fraction of massive galaxies that contains an AGN. Moreover, deep *Chandra* X-ray observations indicate that a substantial fraction of AGNs might be heavily obscured (Mushotzky et al. 2000), and might prove difficult to identify at optical or near-IR wavelengths. Because the life-time of a powerful radio source ( $10^7 - 10^8$  y; Blundell & Rawlings 1999b) is short compared to the Hubble time, a substantial fraction of massive galaxies should be going through a period of radio inactivity, and can only be found from non-radio selected surveys. An approach made possible with the advent of deep X-ray surveys with *Chandra* and *XMM-Newton* is to use the X-ray emission as a signpost of nuclear activity. This provides a powerful alternative for radio observations, although the survey areas covered are still small. From deep multi-wavelength observations of the Hawai'i Deep Survey Field SSA13, Barger et al. (2001) find that  $7_{-3}^{+5}\%$  of the optically luminous galaxies ( $-22.5 > M_I > -24$ ) are indeed X-ray sources.

## 5. REPERCUSSIONS FOR HZRG SEARCHES

The original goal of the imaging programme was to identify our USS sources as promising high redshift radio galaxy targets for subsequent optical spectroscopy. We find that due to the red  $R - K$  colors of the host galaxies, near-IR imaging is a far more efficient technique for obtaining HzRG identifications than optical imaging. Near-IR imaging leads to an almost complete identification rate, and provides an approximate photometric redshift by means of the Hubble  $K - z$  diagram, or, potentially, from a modified  $K - z - P_{\text{radio}}$  relation. Figure 3 shows that the majority of the  $K$ -band images are relatively bright, suggesting that the average redshift of our sample is relatively moderate. To examine this quantitatively, we first transformed the  $8''$  diameter apertures to 64 kpc metric apertures using the average correction of  $K_{64\text{kpc}} = K(8'') + 0.2$ . We then used the fit of the  $K_{64\text{kpc}}$  versus  $\log_{10}(z)$  relation as obtained in §4 to determine the predicted redshift of these objects. Although this is a severe over-simplification

which ignores the scatter in the  $K - z$  relation, and is based on only 13% of the total number of sources in our USS sample, it can provide a first estimate of the redshift distribution of the 81 objects detected at  $K$ -band.

Figure 11 shows this predicted redshift distribution. The median predicted redshift from this sample is 2.06, while the mean is  $\bar{z} = 2.25$ . This median redshift is consistent with the rather steep surface brightness profiles typical of  $z < 3$  radio galaxies (see §3.3). Figure 11 also shows the distribution of the spectroscopic redshifts obtained, which has a mean/median at  $z \simeq 2.5$ . This difference illustrates the advantage of using an additional faint near-IR magnitude selection criterion to increase the chances for finding very high redshift radio galaxies.

The distributions in Figures 4 and 11 suggest that the majority of the sources in our sample are very red objects or even EROs at  $0.5 \lesssim z \lesssim 2.5$  with a tail of very high redshift radio galaxies. Wide-field surveys of EROs have indeed shown that the density of ERO increases with  $K$ -band magnitude out to their completeness limit of  $K \sim 19$  (e.g. Daddi et al. 2000). Because the imaging sub-sample selects objects at  $K$ -band, and a number of objects were even pre-selected to have faint  $R$ -band magnitudes, our sample includes a large number of very red objects and EROs that happen to be radio-loud. This population might represent more than half of our total sample, suggesting that very red objects at  $z \sim 1.5$  are probably important contributors to galaxy counts in steep-spectrum radio-selected samples. These red objects generally have  $18 < K < 20$ , explaining our increased success in finding  $z > 3$  radio galaxies by concentrating on the  $K > 20$  identifications.

## 6. CONCLUSIONS

We have obtained 83 optical images, and 85 near-IR images of sources selected from our USS sample. Our main conclusions from these observations are:

- $\sim 50\%$  of the objects are detected in the optical images down to  $R \sim 24 - 25$ .
- 94% of the objects are detected in the near-IR  $K$ -band down to  $K \sim 22$ , with a mean  $\bar{K} = 19.26$  in a  $2''$  diameter aperture. One of the non-detections is due to the limited sensitivity of the radio map, while the other 3 are intrinsically faint  $K$ -band sources, 1 having  $K \gtrsim 19$ , and 2 having  $K \gtrsim 22$ .
- The distribution of  $R - K$  colors shows that at least 1/3 have  $R - K > 5$ , and at least 4 objects ( $> 10\%$ ) are EROs with  $R - K > 6$ .
- The  $K > 20$  identifications appear only associated with small ( $\lesssim 2''$ ) radio sources.
- The  $K$ -band morphologies show mostly compact objects typical of  $z \lesssim 3$  radio galaxies.
- The major axes of the  $K$ -band morphologies, as determined from the fitting of ellipsoidal isophotes are preferentially oriented along the radio axes. This provides further evidence for the existence of a near-IR/radio alignment effect.
- The 22 objects from our sample with known  $z$  and  $K$  obey the same relationship in the Hubble  $K - z$  diagram as previous radio samples, but with a larger scatter.
- The scatter may well be dominated by the radio power, which is correlated with the deviation from a linear fit to

the  $\log_{10}(z)$  vs.  $K_{64kpc}$  relation with a 99.94% significance level. This indicates that the most powerful radio sources are located in the most massive host galaxies, probably due to a mutual correlation of galaxy mass and radio power on the mass of the central black hole. The previously known HzRGs were drawn from samples which included only the most powerful radio sources, giving rise to a tighter correlation in the  $K - z$  diagram.

- A comparison between the  $K - z$  relation of radio-loud and radio-quiet galaxies determined from the HDF-North and the Hawaii survey shows that the radio-loud galaxies define the luminous envelope of the  $K$ -band magnitudes at  $z \lesssim 1$ , while at  $z \gtrsim 1$ , the radio-loud galaxies are  $\gtrsim 2$  magnitudes brighter. This is amongst the strongest evidence to date that radio galaxies trace the most massive forming stellar populations at high redshifts.

- Radio galaxies generally have redder  $R - K$  colors than optically selected galaxies from the HDF, especially at  $z \lesssim 2$ . This indicates radio host galaxies also contain more evolved stellar populations.

- Some of the brightest objects in the  $K$ -band from the optically selected surveys appear to contain AGN, suggesting that the fraction of massive galaxies containing AGN is quite high. However, a much larger  $K$ -band selected sample of high redshift galaxies would be needed to estimate this fraction.

- The HzRGs with the faintest  $K$ -band identifications may be extremely dusty and/or at extremely high ( $z > 7$ ) redshifts. We have therefore embarked on a program to obtain near-IR spectroscopy at Keck and sub-mm observations at JCMT/IRAM to investigate this in more detail and will report on the results in a forthcoming paper (Reuland et al. 2001).

We thank Mike Brown for letting us use a severely crippled NIRC camera on Keck I for half a night (1999 September 22) when the instrument was of no use to his demanding Solar System observations, while it could be employed for our simple purpose of  $K$ -band galaxy identifications in the early Universe. We thank Mark Dickinson for providing the catalog of redshifts and  $K$ -band magnitudes in the HDF-North, and for helpful comments on the  $K - z$  diagram. We thank Roy Gal for obtaining Palomar 60'' images needed for the astrometry of a few of the fields. We are grateful for the excellent help provided by the staff of the Lick, Keck, ESO, CTIO, and WHT telescopes. We thank Damien Le Borgne, Brigitte Rocca-Volmerange, Michel Fioc and Philip Best for useful discussions, and the referee Arjun Dey for constructive comments that have improved the paper. This research made use of the NASA/IPAC Extragalactic Database (NED) which is operated by the Jet Propulsion Laboratory, California Institute of Technology, under contract with the National Aeronautics and Space Administration. The work by C.D.B., W.v.B., and S.A.S. at IGPP/LLNL was performed under the auspices of the US Department of Energy by University of California Lawrence Livermore National Laboratory under contract W-7405-ENG-48. This work was supported in part by the Formation and Evolution of Galaxies network set up by the European Commission under contract ERB FMRX-CT96-086 of its TMR programme, and by a Marie Curie Fellowship of the European

Community programme “Improving Human Research Potential and the Socio-Economic Knowledge Base” under contract number HPMF-CT-2000-00721.

## REFERENCES

- Archibald, E., Dunlop, J., Hughes, D., Rawlings, S., Eales, S., & Ivison, R. 2001, *MNRAS*, 323, 417
- Armus, L., Soifer, B., Murphy, T., Neugebauer, G., Evans, A., & Matthews, K. 1998a, *ApJ*, 495, 276
- Armus, L., Matthews, K., Neugebauer, G., & Soifer, B. 1998b, *ApJ*, 506, L89
- Barger, A., Cowie, L., Mushotzky, R., & Richards, E. 2001, *AJ*, 121, 662
- Best, P., Longair, M., & Röttgering, H. 1998, *MNRAS*, 295, 549
- Bicknell, G., Sutherland, R., van Breugel, W., Dopita, M., Dey, A., & Miley, G. 2000, *ApJ*, 540, 678
- Blundell, K., Rawlings, S., Eales, S., Taylor, G., & Bradley, A. 1998, *MNRAS*, 295, 265
- Blundell, K., & Rawlings, S. 1999b, *Nature*, 399, 330
- Brandt, W., et al. 1999, *AJ*, 122, 1
- Cardelli, J., Clayton, G., & Mathis, J. 1989, *ApJ*, 345, 245
- Carter, D., & Bridges, T. 1995, *WHT Prime Focus and Auxiliary Port Imaging Manual*
- Casali, M., & Hawarden, T. 1992, *JCMT-UKIRT Newsletter*, 4, 33
- Chambers, K., Miley, G., & van Breugel, W. 1987, *Nature*, 329, 604
- Chambers, K., Miley, G., van Breugel, W., & Huang, J.-S. 1996, *ApJS*, 106, 215
- Cimatti, A., di Serego-Alighieri, S., Fosbury, R., Salvati, M., & Taylor, D. 1993, *MNRAS*, 264, 421
- Cimatti, A., Andreani, P., Röttgering, H., & Tilanus, R. 1998, *Nature*, 392, 895
- Condon, J., Cotton, W., Greisen, E., Yin, Q., Perley, R., Taylor, G., & Broderick, J. 1998, *AJ*, 115, 1693
- Cowie, L., et al. 1994a, *ApJ*, 432, L83
- Cowie, L., et al. 1994b, *ApJ*, 434, 114
- Daddi, E., et al. 2000, *A&A*, 361, 535
- De Breuck, C., van Breugel, W., Minniti, D., Miley, G., Röttgering, H., & Carilli, C. 1999, *A&A*, 352, L51
- De Breuck, C., van Breugel, W., Röttgering, H., & Miley, G. 2000a, *A&AS*, 143, 303 (Paper I)
- De Breuck, C., Röttgering, H., Miley, G., van Breugel, W., & Best, P. 2000b, *A&A*, 362, 519
- De Breuck, C. et al. 2001, *AJ*, 121, 1241 (Paper III)
- Dey, A. & Spinrad, H. 1996, *ApJ*, 459, 133
- Dey, A., van Breugel, W., Vacca, W., & Antonucci, R. 1997, *ApJ*, 490, 698
- Dey, A. 1999a, *The Most Distant Radio Galaxies*, p. 19
- Dey, A., Graham, J., Ivison, R., Smail, I., Wright, G., & Liu, M. 1999b, *ApJ*, 519, 610
- Deutsch, E. W. 1999, *AJ*, 118, 1882
- Dickinson, M. 1999, *After the Dark Ages: When Galaxies were Young (the Universe at  $2 < z < 5$ )*, Ed. S. Holt & E. Smith. 1999, p. 122
- Dickinson, M. 2000, *Proceedings of the XIXth Moriond Astrophysics Meeting*, astro-ph/0004027
- Dickinson, et al. 2001, in preparation
- Dickson, R., Tadhunter, C., Shaw, M., Clark, N., & Morganti, R. 1995, *MNRAS*, 273, L29
- Djorgovski, S. 1985, *PASP*, 97, 1119
- Douglas, J., Bash, F., Bozayan, F., Torrence, G., & Wolfe, C. 1996, *AJ*, 111, 1945
- Dunlop, J., Guiderdoni, B., Rocca-Volmerange, B., Peacock, J., & Longair, M. 1989, *MNRAS*, 240, 257
- Dunlop, J., & Peacock, J. 1993, *MNRAS*, 263, 936
- Eales, S. & Rawlings, S. 1993, *ApJ*, 411, 67
- Eales, S., Rawlings, S., Law-Green, D., Cotter, G., & Lacy, M. 1997, *MNRAS*, 291, 593
- Elston, R., Rieke, G., & Rieke, M. 1988, *ApJ*, 331, L77
- Fernández-Soto, A., Lanzetta, K., & Yahil, A. 1999, *ApJ*, 513, 34
- Fioc, M. & Rocca-Volmerange, B. 1997, *A&A*, 326, 950
- Fioc, M. & Rocca-Volmerange, B. 1999, *PEGASE 2, a metallicity-consistent spectral evolution model of galaxies: the documentation and the code*, <http://www.iap.fr/users/fioc/PEGASE.html>
- Garrett, M., et al. 2001, *A&A*, 366, L5
- Gebhardt, K., et al. 2000, *ApJ*, 539, L13
- Graham, J., & Dey, A. 1996, *ApJ*, 471, 720
- Han, J. & Tian, W. 1999, *A&AS*, 136, 571
- Hornschemeier, A., et al. 2000, *ApJ*, 541, 49
- Ivison, R., et al. 1998, *ApJ*, 494, 211
- Jarvis, M., et al. 2001a, *MNRAS*, 326, 1563
- Jarvis, M., et al. 2001b, *MNRAS*, 326, 1585
- Jedrzejski, R. 1987, *MNRAS*, 226, 747
- Kaplan, D., Condon, J., Arzoumanian, Z., & Cordes, J. 1998, *ApJS*, 119, 75
- Lacy, M., et al. 1994, *MNRAS*, 271, 504
- Lacy, M., Rawlings, S., Hill, G., Bunker, A., Ridgway, S., & Stern, D. 1999, *MNRAS*, 308, 1096
- Lacy, M., Bunker, A., & Ridgway, S. 2000, *AJ*, 120, 68
- Leyshon, G., & Eales, S. 1998, *MNRAS*, 295, 10
- Lilly, S., & Longair, M. 1984, *MNRAS*, 211, 833
- Lilly, S. 1989, *ApJ*, 333, 161
- Longair, M., Best, P., & Röttgering, H. 1995, *MNRAS*, 275, L47
- Matthews, K. & Soifer, B. 1994, in *Proc. Infrared Astronomy with Arrays: The Next Generation*, ed. I. McLean (Dordrecht: Kluwer), p. 239
- McCarthy, P. 1993, *ARA&A*, 31, 693
- McCarthy, P., Kapahi, V., van Breugel, W., Persson, S., Athreya, R., & Subrahmanya, C. 1996, *ApJS*, 107, 19
- McCarthy, P. 1999, *The Most Distant Radio Galaxies*, p. 5
- McLean, I. et al. 1993, *Proc. SPIE*, 1946, 513
- McLure, R., & Dunlop, J. 2000, *MNRAS*, 317, 249
- Miller, J. & Stone, R. 1994, *Lick Observatory Technical Report No. 66*
- Monet, D. et al. 1998, *USNO-SA2.0*, (U.S. Naval Observatory, Washington DC)
- Motohara, K., et al. 2000, *PASJ*, 52, 33
- Mushotzky, R., Cowie, L., Barger, A., & Arnaud, K. 2000, *Nature*, 404, 459
- Oke, J. et al. 1995, *PASP*, 107, 375
- Papadopoulos, P., et al. 2000, *ApJ*, 528, 626
- Papovich, C., Dickinson, M., & Ferguson, H., 2001, *ApJ*, in press, astro-ph/0105087
- Pentericci, L., et al. 1999, *A&A*, 341, 329
- Pentericci, L., McCarthy, P., Röttgering, H., Miley, G., van Breugel, W., & Fosbury, R. 2001, *ApJS*, 135, 63
- Perryman, M., & ESA 1997, *The Hipparcos and Tycho catalogues*, Noordwijk: ESA Publications Division, ESA SP Series 1200
- Persson, S., Murphy, D., Krzeminski, W., Roth, M., & Rieke, M. 1998, *AJ*, 116, 2475
- Rawlings, S. & Saunders, R. 1991, *Nature*, 349, 138
- Rawlings, S., Eales, S., & Lacy, M. 2001, *MNRAS*, 322, 523
- Rengelink, R. et al. 1997, *A&A*, 124, 259
- Reuland, M., et al. 2001, in preparation
- Richards, E., Kellermann, K., Fomalont, E., Windhorst, R., & Partridge, R. 1998, *AJ*, 116, 1039
- Rocca-Volmerange, B. & Guiderdoni, B. 1990, *MNRAS*, 247, 166
- Roche, N., Eales, S. & Rawlings, S. 1998, *MNRAS*, 297, 405
- Röttgering, H., Lacy, M., Miley, G., Chambers, K., & Saunders, R. 1994, *A&AS*, 108, 79
- Röttgering, H., Miley, G., Chambers, K., & Macchetto, F. 1995, *A&AS*, 114, 51
- Savaglio, S., Benetti, S., & Pasquini, L. 1997, *EFOSC1 Operating Manual*
- Schade, D., et al. 1999, *ApJ*, 525, 31
- Schlegel, D., Finkbeiner, D., Davis, M. 1998, *ApJ*, 500, 525
- Simpson, C., Rawlings, S., & Lacy, M. 1999, *MNRAS*, 306, 828
- Simpson, C., Ward, M., Wall, J. 2000, *MNRAS*, 319, 963
- Smail, I., Hogg, D., Yan, L., & Cohen, J. 1995, *ApJ*, 449, L105
- Songaila, A., Cowie, L., Hu, E., & Gardner, J. 1994, *ApJS*, 94, 461
- Spinrad, H., et al. 1998, *AJ*, 116, 2617
- Steidel, C., Adelberger, K., Giavalisco, M., Dickinson, M., & Pettini, M. 1999, *ApJ*, 519, 1
- Stern, D. et al. 1999, *AJ*, 117, 1122
- Stern, D. & Spinrad, H. 1999, *PASP*, 111, 1475
- Tran, H., Cohen, M., Ogle, P., Goodrich, R., & di Serego Alighieri, S. 1998, *ApJ*, 500, 660
- van Breugel, W., Stanford, S. A., Spinrad, H., Stern, D., & Graham, J. R. 1998, *ApJ*, 502, 614 (vB98)
- van Breugel, W., De Breuck, C., Stanford, S. A., Stern, D., Röttgering, H. J. A., & Miley, G. K. 1999, *ApJ*, 518, L61
- Vernet, et al. 2001, *A&A*, 366, 7
- Véron-Cetty, M., & Véron, P. 1996, *A&AS*, 115, 97
- Villani, D., & di Serego Alighieri, S. 1999, *A&AS*, 135, 299
- Waddington, I., Windhorst, R., Cohen, S., Partridge, R., Spinrad, H., & Stern, D. 1999, *ApJ*, 526, L77
- Weymann, R. et al. 1998, *ApJ*, 505, L95
- Wieringa, M., & Katgert, P. 1992, *A&AS*, 93, 399
- Williams, R., et al. 1996, *AJ*, 112, 1335
- Willott, C., Rawlings, S., & Blundell, K. 2001a, *MNRAS*, 324, 1
- Willott, C., Rawlings, S., & Blundell, K. 2001b, *Proc. "QSO hosts and their environments"*, astro-ph/0104118

TABLE 1  
RECENT RADIO REDSHIFT SURVEYS

Survey	Selection in $S$ [mJy]	Selection in $\alpha$	Median $S_{1400}$ [mJy]	Mean $S_{1400}$ [mJy]	% $z_{spec}$	Mean $z$	# sources	Reference
MRC	$S_{408} > 950$	All	463	641	67.0	0.74	558	1
6CE	$2000 < S_{151} < 3930$	All	391	427	94.9	1.14	59	2
MP	$S_{408} > 700$ ; $S_{4850} > 35$	$\alpha_{408}^{4850} < -1.20$	311	395	15.5	0.88	58	3
USS	varies <sup>a</sup>	$\alpha < -1.0^a$	281	318	2.3	1.27	1165	4
7C-III	$S_{151} > 500$	All	184	211	81.5	1.19	54	5
6C*	$960 < S_{151} < 2000$	$\alpha_{151}^{4850} < -0.98$	131	127	100.0	1.96	29	6
TN	$S_{365} > 150$ ; $S_{1400} > 10$	$\alpha_{365}^{1400} < -1.30$	74	118	7.1	2.10	268	3
WN	$S_{325} > 18$ ; $S_{1400} > 10$	$\alpha_{325}^{1400} < -1.30$	18	41	4.4	1.87	343	3

<sup>a</sup>The USS sample of Röttgering et al.(1994) consists of 9 sub-samples, each with different flux density and spectral index limits. See Table 4 of Röttgering et al.(1994) for details.

References. — (1) McCarthy et al. (1996); (2) Rawlings, Eales, & Lacy (2001); (3) De Breuck et al. (2000a); (4) Röttgering et al. (1994); (5) Lacy et al. (1999); (6) Jarvis et al. (2001a)

TABLE 2  
OBSERVING SESSIONS

Run	UT Date	Telescope	Instrument	Photometric?	Seeing
L3	1996 Apr 19	Lick 3m	Kast	no	1''8
L6	1996 Nov 11	Lick 3m	Kast	yes	1''3
L7	1997 Jan 7-9	Lick 3m	Kast	no	2''-3''
E2	1997 Mar 5-6	ESO 3.6m	EFOSC1	yes	1''3
E3	1997 Apr 9-11	ESO 3.6m	EFOSC1	yes	1''4
W4	1997 May 1-2	WHT 4.2m	Prime-focus	yes	0''9
L8	1997 May 6-7	Lick 3m	Kast	yes	1''7
L9	1997 Jun 6-8	Lick 3m	Kast	yes	1''1-2''
L10	1997 Aug 8	Lick 3m	Kast	no	1''2-1''5
K4	1997 Sep 10-11	Keck 10m	NIRC	yes	0''4-0''5
C1	1998 Feb 16	CTIO 4m	CIRIM	yes	0''5
K7	1998 Apr 18-19	Keck 10m	NIRC	yes	0''4-0''6
L13	1998 Aug 23-24	Lick 3m	Kast	yes	1''3
C2	1998 Sep 1-4	CTIO 4m	CIRIM	partly	0''6-1''
L15	1998 Oct 18-19	Lick 3m	Kast	partly	1''0-1''3
K9	1998 Dec 19-20	Keck 10m	LRIS	yes	0''7
W5	1999 May 17-19	WHT 4.2m	Prime-focus	yes	1''0
K10	1999 May 22-23	Keck 10m	NIRC	yes	0''3-0''4
K12	1999 Sep 23-24	Keck 10m	NIRC	no <sup>a</sup>	0''4-0''7
P1	1999 Oct 13	Palomar 60''	CCD13	yes	0''9
K13	2000 Jan 30	Keck 10m	NIRC	yes	0''6

<sup>a</sup>Affected by instrumental problems, see §2.1.1



TABLE 3  
JOURNAL OF IMAGING OBSERVATIONS

Source	$z$	Run	Filter	$t_{exp}$ (s)
WN J0000+4654	...	K12	$K$	780
WN J0007+3641	...	L13	$r_S$	600
WN J0034+4142	...	L13	$r_S$	3000
		K12	$K$	1020
WN J0040+3857	2.605	L15	$r_S$	2700
MP J0100-6403	...	C2	$K$	1800
TN J0102-1055	...	K12	$K$	780
MP J0114-3302	...	C2	$K$	1920
WN J0117+3715	...	K12	$K$	840
TN J0121+1320	3.516	L7	$r_S$	1800
		K4	$K_S$	3840
MP J0130-8352	...	C2	$K$	1920
WN J0137+3250	...	L15	$r_S$	3600
MP J0141-6941	...	C2	$K$	1920
WN J0155+8036	...	L15	$r_S$	2100
TN J0201-1302	...	K12	$K$	1560
MP J0202-5425	...	C2	$K$	3840
TN J0205+2242	3.506	L7	$r_S$	1980
		K4	$K_S$	1920
TN J0218+0844	...	L10	$r_S$	900
WN J0231+3600	3.079	K9	$I$	720
MP J0249-4145	...	C2	$K$	840
WN J0303+3733	2.506	L15	$r_S$	3000
WN J0305+3525	...	K9	$I$	960
		K12	$K$	2280
WN J0310+3644	...	K9	$I$	900
MP J0340-6507	...	C2	$K$	960
WN J0346+3039	...	K12	$K_S$	600
WN J0359+3000	...	L13	$r_S$	3000
		K12	$K_S$	540
TN J0402+1007	...	L7	$r_S$	2280
		K4	$K_S$	1920
TN J0410+1019	...	K12	$K$	1320
MP J0449-5449	...	C2	$K$	720
TN J0452-1737	2.256	L7	$r_S$	1800
		K4	$K_S$	960
TN J0517-0641	...	E2	$R$	600
WN J0528+6549	...	K13	$K$	1920
WN J0538+7348	...	L15	$r_S$	3000
		K13	$K$	1920
TN J0552-0433	...	E2	$R$	600
MP J0601-3926	...	C1	$K_S$	3840
WN J0610+6611	...	K13	$K'$	1920
WN J0617+5012	3.153	L6	$r_S$	2550
		K4	$K_S$	2880
WN J0633+4653	...	L15	$r_S$	3600
WN J0716+5107	...	L15	$r_S$	3300
		K13	$K'$	1920
WN J0717+4611	1.462	L6	$r_S$	900
WN J0741+5611	...	L7	$r_S$	2400
		K7	$K$	1500
WN J0747+3654	2.992	L7	$r_S$	900
		K13	$K'$	1260
WN J0813+4828	1.274	L7	$r_S$	2700
		K7	$K_S$	1920
TN J0837-1053	...	E2	$R$	600
TN J0855-0000	...	E2	$R$	900
TN J0856-1510	...	E3	$R$	900
		K13	$K'$	3360
TN J0910-2228	...	E3	$R$	900
TN J0920-0712	2.760	E3	$R$	300
TN J0924-2201	5.19	E3	$R$	900
		K7	$K_S$	3840
TN J0936-2243	1.479	E3	$R$	900
		K7	$K_S$	960
TN J0941-1628	1.644	E2	$R$	900
WN J0948+6305	...	L15	$r_S$	2100
WN J1015+3038	0.54:	K7	$K_S$	960
TN J1026-2116	...	E3	$R$	900
		K7	$K$	960
TN J1033-1339	2.425	E3	$R$	900
		K10	$K_S$	2880
TN J1043-1718	...	E3	$R$	900
TN J1049-1258	...	E2	$R$	600
		K7	$K$	900
WN J1053+5424	...	L7	$r_S$	3240
		K10	$K_S$	1920
WN J1055+3047	...	L7	$r_S$	2400
		K7	$K_S$	960
TN J1102-1651	2.111	E2	$R$	900
TN J1112-2948	3.09	E2	$R$	600

TABLE 3—*Continued*

Source	$z$	Run	Filter	$t_{exp}$ (s)
WN J1115+5016	2.54	L7	$r_S$	2100
		K7	$K_S$	960
TN J1123–2154	4.109	E2	$R$	900
		K7	$K_S$	960
WN J1123+3141	3.217	L3	$r_S$	2700
		K10	$K_S$	1920
TN J1146–1052	...	W5	$R$	600
TN J1148–0901	...	W5	$R$	600
TN J1151–3013	...	E3	$R$	900
		K10	$K_S$	1920
TN J1159–1629	...	E3	$R$	600
WN J1224+5436	...	W5	$R$	600
		K10	$K$	1920
WN J1242+3915	2.131	L7	$r_S$	3840
		K7	$K_S$	960
WN J1258+3212	...	L9	$r_S$	3300
		K13	$K'$	1260
WN J1314+3649	...	W4	$R$	600
		K7	$K$	960
WN J1333+3037	1.213	W4	$R$	600
TN J1338–1942	4.11	E3	$R$	600
		K7	$K$	3840
WN J1355+3848	...	W4	$R$	600
		K10	$K_S$	1920
WN J1420+6735	...	W5	$R$	600
		K10	$K$	1920
WN J1421+3103	...	W5	$R$	600
TN J1428+2425	...	K10	$K_S$	1920
WN J1433+3044	...	W4	$R$	600
		K7	$K_S$	960
WN J1450+3534	...	W5	$R$	600
		K10	$K$	1920
WN J1500+3613	...	L9	$r_S$	1800
TN J1506+2728	...	K10	$K_S$	1920
WN J1525+3010	...	W4	$R$	600
		K7	$K$	1020
WN J1529+3454	...	W5	$R$	600
WN J1543+3512	0.703	W4	$R$	600
WN J1546+3005	...	W4	$R$	600
WN J1546+3935	...	W4	$R$	600
WN J1550+3830	...	L9	$r_S$	1200
		K10	$K$	1920
WN J1555+4011	...	K10	$K_s$	960
WN J1604+5505	...	K10	$K_S$	1920
TN J1634–2222	...	E3	$R$	60
WN J1645+4413	...	K10	$K_S$	960
WN J1718+5823	...	L13	$r_S$	3600
WN J1731+4640	...	K10	$K_s$	1860
WN J1731+4654	...	L10	$r_S$	900
		K10	$K_S$	840
MP J1755–6916	2.551	C2	$K$	2880
MP J1758–6738	2.026	C2	$K$	1560
WN J1802+3948	...	L13	$r_S$	3600
WN J1804+3048	...	K10	$K_S$	960
WN J1818+3852	...	K10	$K$	1920
WN J1818+6144	...	K10	$K$	960
WN J1829+5945	...	L13	$r_S$	660
WN J1830+6422	...	L13	$r_S$	3900
WN J1836+5210	...	K10	$K_s$	960
WN J1859+5900	...	W5	$R$	600
WN J1859+5416	...	W5	$R$	600
WN J1911+6342	3.590	K10	$K$	960
WN J1917+6635	...	K10	$K$	960
MP J1929–3732	0.748	C2	$K$	2880
TN J1941–1952	...	K12	$K$	840
TN J1954–1207	...	K10	$K$	960
MP J2003–8340	1.169	C2	$K$	3840
TN J2007–1316	...	K12	$K_S$	780
TN J2008–1344	...	P1	$r$	900
TN J2009–3040	...	K10	$K$	1440
TN J2028–1934	...	P1	$r$	900
		K12	$K_s$	1320
WN J2044+7044	...	L15	$r_S$	3300
		K10	$K_s$	1560
MP J2045–6018	1.464	C2	$K$	2460
MP J2048–5750	1.262	C2	$K$	2880
MP J2126–5439	...	C2	$K$	2880
WN J2213+3411	...	L13	$r_S$	3900
		K12	$K_S$	1560
WN J2221+3800	...	P1	$r$	900
WN J2222+3305	...	L15	$r_S$	600

TABLE 3—*Continued*

Source	$z$	Run	Filter	$t_{exp}(s)$
MP J2226–7654	...	C2	$K$	1680
WN J2250+4131	...	K12	$K$	1560
WN J2313+4053	2.99	L15	$r_S$	120
WN J2313+4253	...	K12	$K$	1080
TN J2314+2053	...	L10	$r_S$	840
		K12	$K$	1800
MP J2352–6154	...	C2	$K$	3840

TABLE 4  
OBSERVATIONAL SETUP

Telescope	Instrument	Filter	FOV <sup>a</sup>	Pixel scale
Keck	LRIS	$I$	$6' \times 7'.8$	$0''.212 \pm 0''.001$
WHT	PFIP+EEV42	$R$	$8' \times 16'$	$0''.236 \pm 0''.001$
	PFIP+LOR2	$R$	$9' \times 9'$	$0''.2631 \pm 0''.0006$
ESO 3.6m	EFOSC1	$R$	$5'.2 \times 5'.2$	$0''.6075 \pm 0''.0007$
Lick 3m	Kast	$r_S$	$145'' \times 145''$	$0''.789 \pm 0''.0035$
Palomar 60''	CCD13	$r$	$12'.9 \times 12'.9$	$0''.3786 \pm 0''.0005$
Keck	NIRC	$K, K_S, K'$	$38''.4 \times 38''.4$	$0''.1516 \pm 0''.0016$
CTIO 4m	CIRIM	$K, K_S$	$54'' \times 54''$	$0''.219 \pm 0''.007$

<sup>a</sup>Field of view of a single exposure; the combined images might be significantly larger due to the dithering applied.

TABLE 5  
ASTROMETRIC DATA

Source		$\alpha_{J2000}$ h m s	$\delta_{J2000}$ ° ' "
WN J0000+4654	Radio	00 00 28.88	+46 54 40.7
	IR	00 00 28.93	+46 54 40.9
	A <sup>IR</sup>	00 00 29.25	+46 54 53.8
WN J0007+3641	Radio	00 07 02.92	+36 41 55.9
	Opt	00 07 02.80	+36 41 55.8
	A <sup>opt</sup>	00 07 04.92	+36 42 09.3
WN J0034+4142	Radio	00 34 29.21	+41 42 09.5
	IR	00 34 29.10	+41 42 15.7
	A <sup>IR</sup>	00 34 30.38	+41 42 06.5
WN J0040+3857	Radio	00 40 56.23	+38 57 30.0
	Opt	00 40 56.19	+38 57 29.8
	A <sup>opt</sup>	00 40 59.27	+38 57 19.8
MP J0100–6403	Radio	01 00 32.42	–64 03 13.6
	IR	01 00 32.27	–64 03 14.4
	A <sup>IR</sup>	01 00 29.39	–64 03 11.4
TN J0102–1055	Radio	01 01 59.99	–10 55 56.0
	IR	01 02 00.01	–10 55 54.5
	A <sup>IR</sup>	01 02 00.76	–10 56 10.1
MP J0114–3302	Radio	01 14 37.06	–33 02 10.2
	IR	01 14 36.64	–33 02 11.3
	A <sup>IR</sup>	01 14 35.69	–33 02 20.2
WN J0117+3715	Radio	01 17 10.02	+37 15 16.3
	IR	01 17 10.10	+37 15 16.3
	A <sup>IR</sup>	01 17 09.61	+37 15 06.2
TN J0121+1320	Radio	01 21 42.74	+13 20 58.3
	IR	01 21 42.76	+13 20 58.1
	A <sup>IR</sup>	01 21 44.52	+13 20 58.5
MP J0130–8352	Radio	01 30 07.46	–83 52 29.6
	IR	01 30 08.88	–83 52 33.0
	A <sup>IR</sup>	01 30 08.46	–83 52 17.5
WN J0137+3250	Radio	01 36 59.85	+32 50 40.7
	Opt	01 36 59.86	+32 50 38.5
	A <sup>opt</sup>	01 37 03.40	+32 51 05.9
MP J0141–6941	Radio	01 41 55.18	–69 41 33.0
	IR	01 41 55.01	–69 41 33.1
	A <sup>IR</sup>	01 41 56.70	–69 41 15.3
WN J0155+8036	Radio	01 55 43.77	+80 36 48.1
	Opt	01 55 43.85	+80 36 50.3
	A <sup>opt</sup>	01 55 39.96	+80 36 29.2
TN J0201–1302	Radio	02 01 15.80	–13 02 19.4
	IR	02 01 15.75	–13 02 18.8
	A <sup>IR</sup>	02 01 14.26	–13 02 28.5
MP J0202–5425	Radio	02 02 56.25	–54 25 13.3
	IR	02 02 56.25	–54 25 13.7
	A <sup>IR</sup>	02 02 53.69	–54 25 23.7
TN J0205+2242	Radio	02 05 10.69	+22 42 50.2
	IR	02 05 10.71	+22 42 51.1
	A <sup>IR</sup>	02 05 11.78	+22 42 34.2
TN J0218+0844	Radio	02 18 25.56	+08 44 31.3
	A <sup>opt</sup>	02 18 25.02	+08 43 51.5
WN J0231+3600	Radio	02 31 11.48	+36 00 26.6
	Opt	02 31 11.13	+36 00 23.8
	A <sup>opt</sup>	02 31 09.95	+36 00 52.0
MP J0249–4145	Radio	02 49 10.08	–41 45 36.3
	A <sup>IR</sup>	02 49 10.41	–41 45 55.8
WN J0303+3733	Radio	03 03 26.01	+37 33 41.6
	Opt	03 03 26.09	+37 33 41.0
	A <sup>opt</sup>	03 03 26.40	+37 34 10.6
WN J0305+3525	Radio	03 05 47.42	+35 25 13.4
	IR	03 05 47.58	+35 25 13.3
	A <sup>IR</sup>	03 05 47.76	+35 25 33.2
WN J0310+3644	Radio	03 10 54.80	+36 44 02.5
	Opt	03 10 54.77	+36 44 03.2
	A <sup>opt</sup>	03 10 53.38	+36 44 18.7
MP J0340–6507	Radio	03 40 44.92	–65 07 07.3
	IR	03 40 45.33	–65 07 08.0
	A <sup>IR</sup>	03 40 50.15	–65 07 00.7

TABLE 5—*Continued*

Source		$\alpha_{J2000}$ h m s	$\delta_{J2000}$ ° ' "
WN J0346+3039	Radio	03 46 42.60	+30 39 51.0
	IR	03 46 42.55	+30 39 50.7
	A <sup>IR</sup>	03 46 43.67	+30 39 35.5
WN J0359+3000	Radio	03 59 12.86	+30 00 51.7
	IR	03 59 12.89	+30 00 55.0
	A <sup>IR</sup>	03 59 11.44	+30 00 43.1
TN J0402+1007	Radio	04 02 34.44	+10 07 14.9
	IR	04 02 34.44	+10 07 15.1
	A <sup>IR</sup>	04 02 35.13	+10 06 52.5
TN J0410+1019	Radio	04 10 40.52	+10 19 13.6
	IR	04 10 40.56	+10 19 13.8
	A <sup>IR</sup>	04 10 40.38	+10 19 35.3
MP J0449−5449	Radio	04 49 04.66	−54 49 10.1
	IR	04 49 04.73	−54 49 07.9
	A <sup>IR</sup>	04 49 02.08	−54 48 38.6
TN J0452−1737	Radio	04 52 26.66	−17 37 54.0
	IR	04 52 26.68	−17 37 54.0
	A <sup>IR</sup>	04 52 26.30	−17 37 35.9
TN J0517−0641	Radio	05 17 36.89	−06 41 14.6
	Opt	05 17 36.85	−06 41 14.5
	A <sup>opt</sup>	05 17 38.25	−06 40 57.0
WN J0528+6549	Radio	05 28 46.07	+65 49 57.3
	IR	05 28 46.03	+65 49 58.0
	A <sup>IR</sup>	05 28 44.65	+65 49 48.6
WN J0538+7348	Radio	05 38 25.59	+73 48 39.6
	IR	05 38 25.61	+73 48 39.6
	A <sup>IR</sup>	05 38 35.39	+73 48 42.8
TN J0552−0433	Radio	05 52 14.38	−04 33 28.8
	Opt	05 52 14.30	−04 33 26.9
	A <sup>opt</sup>	05 52 11.68	−04 33 41.2
MP J0601−3926	Radio	06 01 00.77	−39 26 18.1
	IR	06 01 00.74	−39 26 15.5
	A <sup>IR</sup>	06 01 01.67	−39 26 27.0
WN J0610+6611	Radio	06 10 08.59	+66 11 43.1
	IR	06 10 08.47	+66 11 41.9
	A <sup>IR</sup>	06 10 09.61	+66 11 15.0
WN J0617+5012	Radio	06 17 39.37	+50 12 54.7
	IR	06 17 39.40	+50 12 53.2
	A <sup>IR</sup>	06 17 38.96	+50 12 28.3
WN J0633+4653	Radio	06 33 52.18	+46 53 40.5
	A <sup>opt</sup>	06 33 50.38	+46 53 09.2
WN J0716+5107	Radio	07 16 40.50	+51 07 04.7
	IR	07 16 40.50	+51 07 06.4
	A <sup>IR</sup>	07 16 39.32	+51 07 06.6
WN J0717+4611	Radio	07 17 58.49	+46 11 39.1
	Opt	07 17 58.47	+46 11 38.9
	A <sup>opt</sup>	07 18 00.56	+46 11 24.8
WN J0741+5611	Radio	07 41 15.38	+56 11 35.9
	A <sup>opt</sup>	07 41 19.92	+56 11 41.6
	A <sup>IR</sup>	07 41 14.89	+56 11 51.2
WN J0747+3654	Radio	07 47 29.38	+36 54 38.1
	IR	07 47 29.37	+36 54 37.9
	A <sup>IR</sup>	07 47 31.05	+36 54 33.7
WN J0813+4828	Radio	08 13 38.10	+48 28 41.5
	IR	08 13 38.01	+48 28 41.0
	A <sup>IR</sup>	08 13 36.70	+48 28 17.1
TN J0837−1053	Radio	08 37 41.62	−10 53 46.0
	A <sup>opt</sup>	08 37 42.14	−10 54 04.8
TN J0855−0000	Radio	08 55 57.26	−00 00 58.2
	A <sup>opt</sup>	08 55 56.66	−00 00 52.5
TN J0856−1510	Radio	08 56 12.44	−15 10 35.7
	A <sup>opt</sup>	08 56 14.93	−15 10 44.1
TN J0859−1510	Radio	08 56 12.44	−15 10 35.7
	A <sup>IR</sup>	08 56 11.20	−15 10 24.3
TN J0910−2228	Radio	09 10 34.15	−22 28 47.4
	Opt	09 10 34.14	−22 28 46.7
	A <sup>opt</sup>	09 10 32.51	−22 28 26.4

TABLE 5—*Continued*

Source		$\alpha_{J2000}$ h m s	$\delta_{J2000}$ ° ' "
TN J0920–0712	Radio	09 20 22.43	–07 12 17.6
	Opt	09 20 22.41	–07 12 18.4
	A <sup>opt</sup>	09 20 23.35	–07 12 24.4
TN J0924–2201	Radio	09 24 19.92	–22 01 41.5
	IR	09 24 19.93	–22 01 41.4
	A <sup>IR</sup>	09 24 20.48	–22 01 22.6
TN J0936–2243	Radio	09 36 32.53	–22 43 04.9
	IR-North	09 36 32.54	–22 43 01.7
	IR-South	09 36 32.60	–22 43 05.4
	A <sup>IR</sup>	09 36 34.06	–22 43 01.3
TN J0941–1628	Radio	09 41 07.43	–16 28 02.5
	Opt	09 41 07.43	–16 28 02.6
	A <sup>opt</sup>	09 41 08.81	–16 27 50.3
WN J0948+6305	Radio	09 48 40.83	+63 05 42.0
	Opt	09 48 40.82	+63 05 42.2
	A <sup>opt</sup>	09 48 40.10	+63 05 34.0
WN J1015+3038	Radio	10 15 08.92	+30 38 02.0
	IR	10 15 08.93	+30 38 02.9
	A <sup>IR</sup>	10 15 07.15	+30 37 50.5
TN J1026–2116	Radio	10 26 22.37	–21 16 07.7
	IR	10 26 22.39	–21 16 07.7
	A <sup>IR</sup>	10 26 21.92	–21 16 19.6
TN J1033–1339	Radio	10 33 10.70	–13 39 52.0
	IR	10 33 10.67	–13 39 52.2
	A <sup>IR</sup>	10 33 13.05	–13 40 01.5
TN J1043–1718	Radio	10 43 19.42	–17 18 53.5
	Opt	10 43 20.52	–17 18 44.9
	A <sup>opt</sup>	10 43 20.52	–17 18 44.8
TN J1049–1258	Radio	10 49 06.22	–12 58 18.3
	IR	10 49 06.26	–12 58 18.9
	A <sup>IR</sup>	10 49 06.78	–12 58 42.1
WN J1053+5424	Radio	10 53 36.31	+54 24 42.1
	IR	10 53 36.28	+54 24 42.3
	A <sup>IR</sup>	10 53 36.90	+54 24 57.9
WN J1055+3047	Radio	10 55 18.52	+30 47 23.2
	IR	10 55 18.44	+30 47 23.3
	A <sup>IR</sup>	10 55 17.42	+30 47 24.9
TN J1102–1651	Radio	11 02 47.13	–16 51 34.4
	Opt	11 02 47.18	–16 51 35.2
	A <sup>opt</sup>	11 02 46.56	–16 51 00.9
TN J1112–2948	Radio	11 12 23.86	–29 48 06.4
	Opt	11 12 23.98	–29 48 06.6
	A <sup>opt</sup>	11 12 24.54	–29 48 16.2
WN J1115+5016	Radio	11 15 06.87	+50 16 23.9
	IR	11 15 06.90	+50 16 24.5
	A <sup>IR</sup>	11 15 06.79	+50 16 39.8
TN J1123–2154	Radio	11 23 10.15	–21 54 05.3
	IR	11 23 10.18	–21 54 04.8
	A <sup>IR</sup>	11 23 10.85	–21 54 03.4
WN J1123+3141	Radio	11 23 55.85	+31 41 26.1
	IR	11 23 55.88	+31 41 26.5
	A <sup>IR</sup>	11 23 53.28	+31 41 04.7
TN J1146–1052	Radio	11 46 07.21	–10 52 08.6
	Opt	11 46 07.26	–10 52 07.1
	A <sup>opt</sup>	11 46 08.46	–10 52 30.3
TN J1148–0901	Radio	11 48 39.90	–09 01 48.8
	Opt	11 48 39.97	–09 01 49.6
	A <sup>opt</sup>	11 48 42.14	–09 01 41.3
TN J1151–3013	Radio	11 51 59.42	–30 13 40.8
	IR	11 51 59.54	–30 13 40.6
	A <sup>IR</sup>	11 51 59.62	–30 13 48.1
TN J1159–1629	Radio	11 59 53.25	–16 29 48.2
	Opt	11 59 53.30	–16 29 47.9
	A <sup>opt</sup>	11 59 51.29	–16 29 07.8
WN J1224+5436	Radio	12 24 52.35	+54 36 39.9
	IR	12 24 52.32	+54 36 40.1
	A <sup>IR</sup>	12 24 49.21	+54 36 40.2

TABLE 5—*Continued*

Source		$\alpha_{J2000}$ h m s	$\delta_{J2000}$ ° ' "
WN J1242+3915	Radio	12 42 53.09	+39 15 48.6
	IR	12 42 53.08	+39 15 47.6
	A <sup>IR</sup>	12 42 52.02	+39 15 30.2
WN J1258+3212	Radio	12 58 23.62	+32 12 42.4
	IR	12 58 23.63	+32 12 40.8
	A <sup>IR</sup>	12 58 25.64	+32 12 56.4
WN J1314+3649	Radio	13 14 17.86	+36 49 14.6
	IR	13 14 17.80	+36 49 14.6
	A <sup>IR</sup>	13 14 17.74	+36 48 58.9
WN J1333+3037	Radio	13 33 21.20	+30 37 35.1
	Opt	13 33 21.20	+30 37 34.8
	A <sup>opt</sup>	13 33 23.15	+30 37 37.6
TN J1338−1942	Radio	13 38 26.06	−19 42 30.1
	IR	13 38 26.14	−19 42 31.3
	A <sup>IR</sup>	13 38 26.09	−19 42 11.0
WN J1355+3848	Radio	13 55 29.50	+38 48 11.1
	IR	13 55 29.51	+38 48 12.0
	A <sup>IR</sup>	13 55 28.04	+38 48 08.1
WN J1420+6735	Radio	14 20 03.34	+67 35 07.5
	IR	14 20 03.26	+67 35 06.0
	A <sup>IR</sup>	14 20 07.12	+67 34 58.8
TN J1428+2425	Radio	14 28 10.20	+24 25 11.3
	A <sup>IR</sup>	14 28 11.91	+24 25 24.0
WN J1433+3044	Radio	14 33 56.51	+30 44 25.5
	IR	14 33 56.44	+30 44 25.0
	A <sup>IR</sup>	14 33 55.82	+30 44 33.1
WN J1450+3534	Radio	14 50 20.69	+35 34 46.5
	IR	14 50 20.70	+35 34 47.1
	A <sup>IR</sup>	14 50 19.27	+35 34 19.5
WN J1500+3613	Radio	15 00 09.01	+36 13 25.8
	Opt	15 00 09.04	+36 13 27.8
	A <sup>opt</sup>	15 00 07.69	+36 13 51.4
TN J1506+2728	Radio	15 06 35.41	+27 28 55.6
	IR	15 06 35.41	+27 28 56.0
	A <sup>IR</sup>	15 06 33.89	+27 29 10.0
WN J1525+3010	B <sup>IR</sup>	15 06 36.56	+27 28 46.8
	Radio	15 25 01.21	+30 10 30.2
	IR	15 25 01.23	+30 10 29.6
WN J1529+3454	A <sup>IR</sup>	15 25 01.71	+30 10 54.5
	Radio	15 29 41.52	+34 54 31.3
	Opt	15 29 41.45	+34 54 29.9
WN J1543+3512	A <sup>opt</sup>	15 29 39.06	+34 54 29.1
	Radio	15 43 29.49	+35 12 29.7
	Opt	15 43 29.60	+35 12 27.8
WN J1546+3005	A <sup>opt</sup>	15 43 28.27	+35 12 15.1
	Radio	15 46 57.65	+30 05 38.1
	Opt	15 46 57.72	+30 05 39.0
WN J1550+3830	A <sup>opt</sup>	15 46 55.61	+30 05 33.8
	Radio	15 50 19.42	+38 30 14.8
	IR	15 50 19.47	+38 30 13.4
WN J1555+4011	A <sup>IR</sup>	15 50 20.79	+38 29 55.8
	Radio	15 55 02.50	+40 11 58.1
	IR	15 55 02.49	+40 11 58.4
WN J1604+5505	A <sup>IR</sup>	15 55 02.41	+40 11 43.8
	Radio	16 04 21.91	+55 05 45.4
	IR	16 04 21.95	+55 05 45.4
TN J1634−2222	A <sup>IR</sup>	16 04 19.99	+55 05 31.0
	Radio	16 34 49.79	−22 22 12.7
	A <sup>opt</sup>	16 34 50.24	−22 22 29.1
WN J1645+4413	Radio	16 45 35.69	+44 13 42.1
	IR	16 45 35.73	+44 13 43.1
	A <sup>IR</sup>	16 45 37.60	+44 13 42.2
WN J1718+5823	Radio	17 18 18.51	+58 23 21.8
	Opt	17 18 18.51	+58 23 21.8
	A <sup>opt</sup>	17 18 14.16	+58 22 58.0
WN J1731+4640	Radio	17 31 46.10	+46 40 03.1
	IR	17 31 46.02	+46 40 03.4

TABLE 5—*Continued*

Source		$\alpha_{J2000}$ h m s	$\delta_{J2000}$ ° ' "
WN J1731+4654	A <sup>IR</sup>	17 31 48.42	+46 39 40.1
	Radio	17 31 59.63	+46 54 00.2
	A <sup>opt</sup>	17 32 02.07	+46 53 25.2
MP J1755–6916	A <sup>IR</sup>	17 32 02.66	+46 54 08.3
	Radio	17 55 30.23	–69 16 49.8
	IR	17 55 30.02	–69 16 51.7
MP J1758–6738	A <sup>IR</sup>	17 55 30.94	–69 17 07.0
	Radio	17 58 51.25	–67 38 30.5
	IR	17 58 51.29	–67 38 27.9
WN J1802+3948	A <sup>IR</sup>	17 58 51.04	–67 38 40.7
	Radio	18 02 31.65	+39 48 59.6
	A <sup>opt</sup>	18 02 29.76	+39 48 55.8
WN J1804+3048	Radio	18 04 42.01	+30 48 45.0
	IR	18 04 42.03	+30 48 45.4
	A <sup>IR</sup>	18 04 42.07	+30 48 53.7
WN J1818+3852	Radio	18 18 42.17	+38 52 20.4
	IR	18 18 42.02	+38 52 20.7
	A <sup>IR</sup>	18 18 41.01	+38 52 37.0
WN J1818+6144	Radio	18 18 50.55	+61 44 18.4
	IR	18 18 50.58	+61 44 18.3
	A <sup>IR</sup>	18 18 52.08	+61 44 08.0
WN J1829+5945	Radio	18 29 57.26	+59 45 03.2
	A <sup>opt</sup>	18 30 00.12	+59 45 10.7
WN J1830+6422	Radio	18 30 45.82	+64 22 26.3
	A <sup>opt</sup>	18 30 46.86	+64 22 02.2
WN J1836+5210	Radio	18 36 23.22	+52 10 28.4
	IR	18 36 23.20	+52 10 29.3
	A <sup>IR</sup>	18 36 23.04	+52 10 42.8
WN J1859+5900	Radio	18 59 40.34	+59 00 36.8
	Opt	18 59 40.34	+59 00 37.5
	A <sup>opt</sup>	18 59 39.21	+59 01 10.5
WN J1859+5416	Radio	18 59 57.65	+54 16 21.8
	Opt	18 59 57.70	+54 16 22.0
	A <sup>opt</sup>	18 59 58.11	+54 16 14.1
WN J1911+6342	Radio	19 11 49.54	+63 42 09.7
	IR	19 11 49.53	+63 42 10.5
	A <sup>IR</sup>	19 11 52.90	+63 41 56.1
WN J1917+6635	Radio	19 17 35.50	+66 35 38.5
	IR	19 17 35.62	+66 35 38.3
	A <sup>IR</sup>	19 17 40.24	+66 35 39.8
MP J1929–3732	Radio	19 29 8.51	–37 32 48.8
	IR	19 29 08.60	–37 32 47.8
	A <sup>IR</sup>	19 29 10.55	–37 32 38.4
TN J1941–1952	Radio	19 41 00.07	–19 52 14.0
	IR	19 41 00.02	–19 52 14.3
	A <sup>IR</sup>	19 41 00.30	–19 52 20.4
TN J1954–1207	Radio	19 54 24.15	–12 07 48.7
	IR	19 54 24.24	–12 07 48.5
	A <sup>IR</sup>	19 54 24.17	–12 07 39.3
MP J2003–8340	Radio	20 03 30.73	–83 41 00.0
	IR	20 03 30.43	–83 40 58.7
	A <sup>IR</sup>	20 03 36.28	–83 40 55.0
TN J2007–1316	Radio	20 07 53.23	–13 16 43.6
	IR	20 07 53.23	–13 16 43.6
	A <sup>IR</sup>	20 07 54.30	–13 16 52.7
TN J2008–1344	Radio	20 08 07.48	–13 44 17.8
	A <sup>opt</sup>	20 08 06.06	–13 44 21.2
TN J2009–3040	Radio	20 09 48.13	–30 40 07.0
	IR	20 09 48.08	–30 40 07.4
	A <sup>IR</sup>	20 09 47.90	–30 39 52.9
TN J2028–1934	Radio	20 28 48.57	–19 34 03.2
	IR	20 28 48.66	–19 34 01.1
	A <sup>IR</sup>	20 28 50.09	–19 33 51.6
WN J2044+7044	Radio	20 44 57.80	+70 44 03.8
	IR	20 44 57.93	+70 44 04.2
	A <sup>IR</sup>	20 44 53.38	+70 44 11.0
MP J2045–6018	Radio	20 45 21.82	–60 18 51.4



TABLE 5—*Continued*

Source		$\alpha_{J2000}$ h m s	$\delta_{J2000}$ ° ' "
MP J2048–5750	IR	20 45 21.31	–60 18 54.7
	A <sup>IR</sup>	20 45 19.38	–60 18 43.5
	Radio	20 48 36.64	–57 50 47.5
	IR	20 48 36.38	–57 50 47.6
MP J2126–5439	A <sup>IR</sup>	20 48 37.92	–57 50 18.0
	Radio	21 26 53.65	–54 39 36.0
	IR	21 26 53.66	–54 39 35.5
	A <sup>IR</sup>	21 26 51.48	–54 39 33.9
WN J2213+3411	Radio	22 13 12.48	+34 11 42.8
	IR	22 13 12.00	+34 11 47.2
	A <sup>IR</sup>	22 13 13.00	+34 12 04.2
	Radio	22 21 49.53	+38 00 38.4
WN J2221+3800	A <sup>opt</sup>	22 21 50.48	+38 00 28.3
	Radio	22 22 15.19	+33 05 44.1
	Opt	22 22 15.11	+33 05 42.7
	A <sup>opt</sup>	22 22 14.51	+33 05 40.1
MP J2226–7654	Radio	22 26 56.90	–76 54 48.0
	IR	22 26 57.37	–76 54 49.6
	A <sup>IR</sup>	22 27 03.57	–76 54 52.1
	Radio	22 50 51.16	+41 31 16.4
WN J2250+4131	IR	22 50 51.15	+41 31 17.2
	A <sup>IR</sup>	22 50 50.62	+41 31 13.7
	Radio	23 13 08.62	+42 53 13.0
	IR	23 13 08.31	+42 53 13.9
TN J2313+4253	A <sup>IR</sup>	23 13 09.42	+42 53 09.9
	Radio	23 14 56.04	+20 53 37.4
	IR	23 14 55.99	+20 53 36.8
	A <sup>IR</sup>	23 14 54.62	+20 53 54.0
MP J2352–6154	Radio	23 52 55.52	–61 54 06.9
	IR	23 52 55.26	–61 54 03.8
	A <sup>IR</sup>	23 53 00.82	–61 54 15.2

Note. — 'Radio' indicates radio source position, 'Opt' optical identification, 'IR' near-IR identification, 'A<sup>opt</sup>' offset star within optical image, and 'A<sup>IR</sup>' offset star within near-IR image.

TABLE 6  
OPTICAL PHOTOMETRY OF USS SOURCES

Source	$z$	Run	Filter	Mag 4''
WN J0007+3641	...	L13	$r_S$	21.6
WN J0034+4142	...	L13	$r_S$	>24.5
WN J0040+3857	2.606	L15	$r_S$	23.3: <sup>†</sup>
TN J0121+1320	3.516	L7	$r_S$	>24
WN J0137+3250	...	L15	$r_S$	23.2: <sup>†</sup>
WN J0155+8036	...	L15	$r_S$	22.3: <sup>†</sup>
TN J0205+2242	3.506	L7	$r_S$	>24
TN J0218+0844	...	L10	$r_S$	>22.5
WN J0231+3600	3.079	K9	$I$	25.0
WN J0303+3733	2.506	L13	$r_S$	23.2
WN J0305+3525	...	K9	$I$	>25
WN J0310+3644	...	K9	$I$	23.0
WN J0359+3000	...	L13	$r_S$	>23.5
TN J0402+1007	...	L7	$r_S$	>24
TN J0452-1737	2.256	L7	$r_S$	>23
TN J0517-0641	...	E2	$R$	24.0
WN J0538+7348	...	L15	$r_S$	>24
TN J0552-0433	...	E2	$R$	22.9
WN J0617+5012	3.153	W3	$R$	>24
WN J0633+4653	...	L15	$r_S$	22.9: <sup>†</sup>
WN J0716+5107	...	L15	$r_S$	>23.5
WN J0717+4611	1.462	L6	$r_S$	21.4
WN J0741+5611	...	L7	$r_S$	>24
WN J0747+3654	2.992	L7	$r_S$	>23: <sup>†</sup>
WN J0813+4828	1.274	L7	$r_S$	23.9
WN J0837-1053	...	E2	$R$	>24.5
TN J0855-0000	...	E2	$R$	>24.5
TN J0856-1510	...	E3	$R$	>23.5
TN J0910-2228	...	E3	$R$	23.0
TN J0920-0712	2.760	E3	$R$	22.4
TN J0924-2201	5.19	E3	$R$	>24
TN J0936-2243	1.479	E3	$R$	>24
TN J0941-1628	1.644	E2	$R$	23.0
WN J0948+6305	...	L15	$r_S$	22.2: <sup>†</sup>
WN J1015+3038	0.54	L8	$r_S$	21.4
TN J1026-2116	...	E3	$R$	>24
TN J1033-1339	2.425	E3	$R$	>24
TN J1043-1718	...	E3	$R$	>24
TN J1049-1258	...	E3	$R$	23.4
WN J1053+5424	...	L7	$r_S$	>24
WN J1055+3047	...	L7	$r_S$	22.8
TN J1102-1651	2.111	E2	$R$	23.7
TN J1112-2948	3.09	E2	$R$	21.5
WN J1115+5016	2.54	L7	$r_S$	>24
TN J1123-2154	4.109	E2	$R$	>24.5
WN J1123+3141	3.217	L7	$r_S$	21.3
TN J1146-1052	...	W5	$R$	23.5
TN J1148-0901	...	W5	$R$	24.2
TN J1151-3013	...	E3	$R$	>24
TN J1159-1629	...	E2	$R$	23.4
WN J1224+5436	...	W5	$R$	24.4
WN J1242+3915	2.131	L7	$r_S$	23.6
WN J1258+3212	...	L9	$r_S$	>24
WN J1314+3649	...	W4	$R$	>26
WN J1333+3037	1.213	W4	$R$	22.5
TN J1338-1942	4.11	E3	$R$	23.0
WN J1355+3848	...	W4	$R$	>25
WN J1420+6735	...	W5	$R$	>25
WN J1433+3044	...	W4	$R$	>25
WN J1450+3534	...	W5	$R$	24.1
WN J1500+3613	...	L9	$r_S$	22.3
WN J1525+3010	...	W4	$R$	25.3
WN J1529+3454	...	W5	$R$	24.1
WN J1543+3512	0.703	W4	$R$	21.2
WN J1546+3935	...	W4	$R$	... <sup>a</sup>
WN J1546+3005	...	W4	$R$	22.4
WN J1550+3830	...	L9	$r_S$	22.8
TN J1634-2222	...	E3	$R$	>23
WN J1718+5823	...	L13	$r_S$	23.0
WN J1731+4654	...	L10	$r_S$	>23: <sup>†</sup>
WN J1802+3948	...	L13	$r_S$	>24
WN J1829+5945	...	L13	$r_S$	>23
WN J1830+6422	...	L13	$r_S$	>24
WN J1859+5900	...	W5	$R$	22.9
WN J1859+5416	...	W5	$R$	20.3
TN J2008-1344	...	P1	$R$	>23
TN J2028-1934	...	P1	$R$	>23
WN J2044+7044	...	L15	$r_S$	>24
WN J2213+3411	...	L13	$r_S$	>24
WN J2221+3800	...	P1	$R$	>23

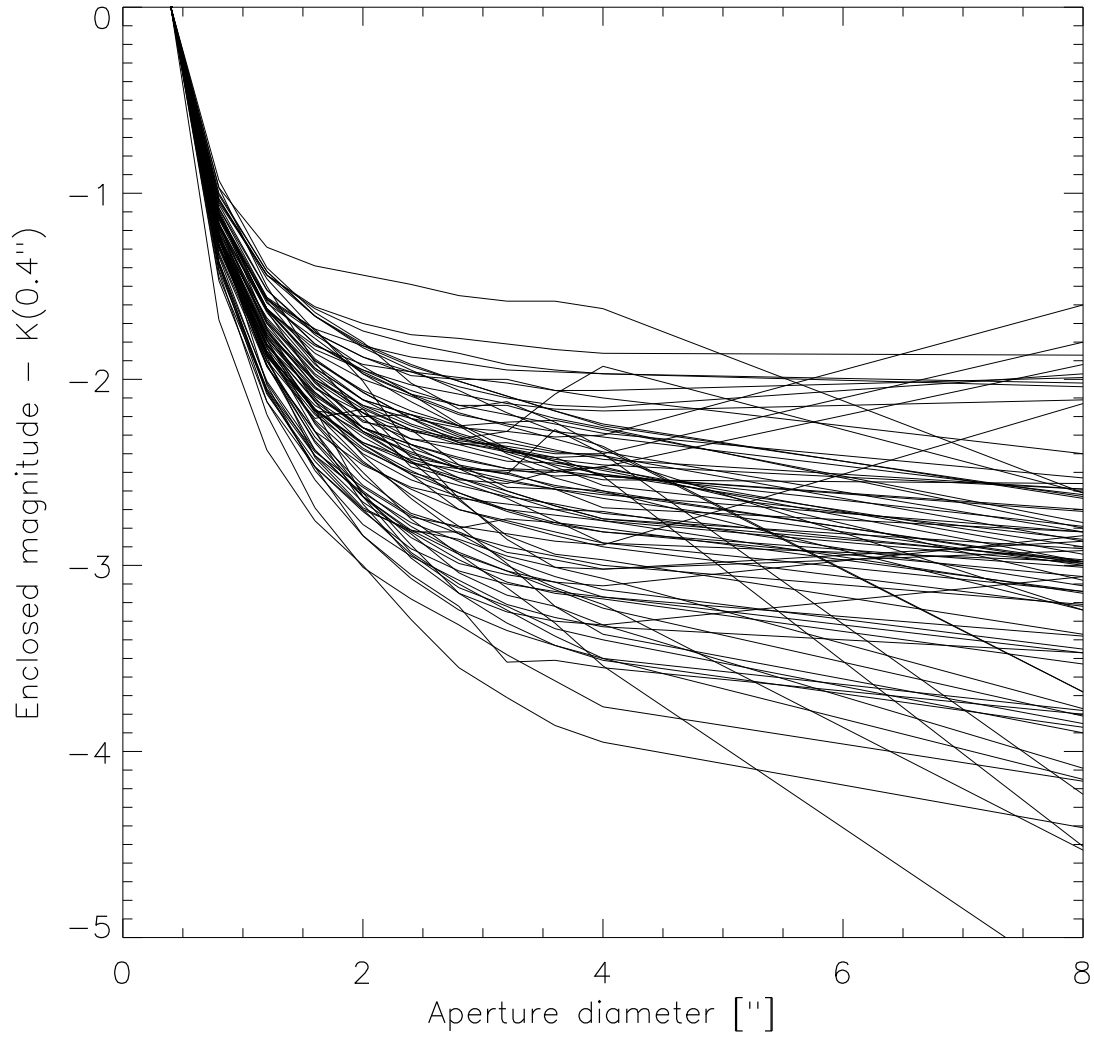


FIG. 1.— Enclosed  $K$ -band magnitude as a function of aperture diameter for our sample of USS radio sources. For the large majority of sources, most of the flux is enclosed in within a  $2''$  aperture.

TABLE 6—*Continued*

Source	$z$	Run	Filter	Mag <sub>4''</sub>
WN J2222+3305	...	L15	$r_S$	21.6 <sup>†</sup>
WN J2313+3842	...	L15	$r_S$	15.8 <sup>†</sup>
TN J2314+2053	...	L10	$r_S$	>23

<sup>†</sup>Estimated from non-photometric conditions.

<sup>a</sup>Nearby bright star prohibits measurement.

Note. — Uncertain values are indicated with a colon.

TABLE 7  
K-BAND PHOTOMETRY AND MORPHOLOGY

Source	z	Run	Filter	A(K) <sup>a</sup>	Mag <sub>2''</sub>	Mag <sub>4''</sub>	Mag <sub>8''</sub>	r <sub>hl</sub>	Ellipticity	PA	Morphology
WN J0000+4654	...	K12	K	0.041	18.49±0.04	17.96±0.04	16.65±0.04	0''/3	...	147°	compact
WN J0034+4142	...	K12	K	0.025	18.80±0.05	18.56±0.05	18.52±0.10	0''/4	0.10	36°	compact
MP J0100-6403	...	C2	K	0.008	19.23±0.15	18.95±0.17	18.61±0.28	...	...	...	low S/N
TN J0102-1055	...	K12	K	0.010	19.45±0.06	19.03±0.07	18.86±0.12	0''/8	0.48	149°	compact
MP J0114-3302	...	C2	K	0.009	18.59±0.11 <sup>†</sup>	17.94±0.10 <sup>†</sup>	17.66±0.15 <sup>†</sup>	...	...	...	low S/N
WN J0117+3715	...	K12	K	0.020	18.22±0.04	17.57±0.04	17.28±0.05	...	...	...	companion
TN J0121+1320	3.516	K4	K <sub>S</sub>	0.014	19.47±0.06	19.00±0.06	18.76±0.07	...	...	85°	companions
MP J0130-8352	...	C2	K	0.047	18.11±0.09 <sup>†</sup>	17.97±0.10 <sup>†</sup>	18.52±0.31 <sup>†</sup>	...	...	...	compact
MP J0141-6941	...	C2	K	0.010	18.06±0.09 <sup>†</sup>	17.62±0.09 <sup>†</sup>	17.36±0.12 <sup>†</sup>	0''/6	...	...	compact
TN J0201-1302	...	K12	K	0.007	16.93±0.03	16.50±0.03	16.29±0.03	...	...	112°	double
MP J0202-5425	...	C2	K	0.009	18.59±0.11	17.55±0.08	15.82±0.06	...	...	...	compact
TN J0205+2242	3.506	K4	K <sub>S</sub>	0.037	19.30±0.06	19.08±0.06	18.77±0.07	0''/1	...	172°	compact
MP J0249-4145	...	C2	K	0.005	>19.0	...	...	...	...	...	non-detection
WN J0305+3525	...	K12	K	0.094	20.84±0.11	20.12±0.10	19.87±0.16	...	...	...	low $\mu$
MP J0340-6507	...	C2	K	0.044	19.07±0.16	18.52±0.17	18.38±0.34	...	...	...	low S/N
WN J0346+3039	...	K12	K <sub>S</sub>	0.163	18.98±0.08 <sup>†</sup>	18.28±0.08 <sup>†</sup>	17.78±0.12 <sup>†</sup>	...	...	...	compact
WN J0359+3000	...	K12	K <sub>S</sub>	0.182	19.03±0.07	18.72±0.10	18.07±0.13	...	...	...	compact
TN J0402+1007	...	K4	K <sub>S</sub>	0.122	17.57±0.04	17.23±0.04	16.99±0.07	0''/4	0.18	28°	compact
TN J0410+1019	...	K12	K	0.140	18.35±0.04	17.98±0.04	17.83±0.05	0''/5	0.22	1°	compact
MP J0449-5449	...	C2	K	0.004	18.02±0.09	17.42±0.09	16.11±0.07	...	...	...	compact
TN J0452-1737	2.256	K4	K <sub>S</sub>	0.018	19.22±0.06	18.77±0.06	18.39±0.09	0''/4	0.18	66°	compact
WN J0528+6549	...	K13	K	0.028	18.81±0.04	18.48±0.04	18.22±0.05	0''/5	0.09	151°	compact
WN J0538+7348	...	K13	K	0.065	19.67±0.06	19.42±0.07	19.23±0.11	0''/2	0.12	115°	compact
MP J0601-3926	...	C1	K	0.020	19.74±0.21	19.47±0.28	18.86±0.38	...	...	...	low S/N
WN J0610+6611	...	K13	K	0.035	18.14±0.04	17.78±0.04	17.42±0.04	0''/4	0.15	29°	compact
WN J0617+5012	3.153	K4	K <sub>S</sub>	0.051	21.49±0.18	20.42±0.13	19.72±0.15	...	...	...	low $\mu$
WN J0716+5107	...	K13	K	0.025	20.35±0.08	20.05±0.08	20.81±0.30	...	0.60	174°	extended
WN J0741+5611	...	K7	K	0.020	>22.5	...	...	...	...	...	non-detection
WN J0747+3654	2.992	K13	K'	0.040	21.13±0.10	20.45±0.08	20.05±0.10	...	...	6°	low $\mu$
WN J0813+4828	1.274	K7	K <sub>S</sub>	0.020	19.18±0.06	19.02±0.06	19.02±0.11	<0''/3	...	112°	compact
TN J0856-1510	...	K13	K	0.022	21.76/22.05	...	...	...	...	...	low S/N
TN J0924-2201	5.19	K7	K <sub>S</sub>	0.021	21.94±0.22	21.71±0.30	19.88±0.15	...	...	...	low $\mu$
TN J0936-2243	1.479	K7	K <sub>S</sub>	0.021	18.62±0.05	18.32±0.05	17.96±0.07	0''/4	0.22	16°	compact
WN J1015+3038	0.54	K7	K <sub>S</sub>	0.010	18.40±0.05	17.78±0.04	17.19±0.04	...	0.21	129°	companions
TN J1026-2116	...	K7	K	0.035	20.41±0.10	19.76±0.11	18.98±0.13	...	...	...	low $\mu$
TN J1033-1339	2.425	K10	K <sub>S</sub>	0.027	19.62±0.06	19.15±0.06	18.86±0.07	...	...	113°	compact
TN J1049-1258	...	K7	K	0.022	19.31±0.05	18.37±0.05	17.90±0.05	...	...	...	interacting
WN J1053+5424	...	K10	K <sub>S</sub>	0.004	20.74±0.12	19.86±0.09	19.21±0.11	...	...	...	low $\mu$
WN J1055+3047	...	K7	K <sub>S</sub>	0.010	19.02±0.06	18.72±0.07	18.40±0.10	<0''/3	...	53°	compact
WN J1115+5016	2.54	K7	K <sub>S</sub>	0.006	20.10±0.09	19.54±0.09	19.22±0.14	...	...	...	low S/N
WN J1123-2154	4.109	K7	K <sub>S</sub>	0.015	20.59±0.14	20.27±0.19	20.41±0.52	...	...	...	low $\mu$
WN J1123+3141	3.217	K10	K <sub>S</sub>	0.007	18.34±0.04	17.84±0.04	17.45±0.04	...	...	...	interacting
TN J1151-3013	...	K10	K <sub>S</sub>	0.018	20.00±0.08	19.77±0.09	19.31±0.12	0''/8	...	170°	compact
WN J1224+5436	...	K10	K	0.005	19.40±0.05	19.14±0.06	18.67±0.07	...	0.17	3°	interacting
WN J1242+3915	2.131	K7	K <sub>S</sub>	0.007	19.14±0.06	18.61±0.06	18.39±0.09	...	0.27	52°	companions
WN J1258+3212	...	K13	K	0.005	19.79±0.06	19.35±0.06	19.19±0.08	0''/4	0.06	156°	compact
WN J1314+3649	...	K7	K	0.004	21.36±0.18	22.07±0.63	...	...	...	...	low S/N
TN J1338-1942	4.11	K7	K	0.036	20.20±0.07	19.95±0.08	19.67±0.13	...	0.37	146°	interacting
WN J1355+3848	...	K10	K <sub>S</sub>	0.008	19.49±0.06	19.28±0.07	19.87±0.18	...	...	80°	compact
WN J1420+6735	...	K10	K	0.009	18.96±0.05	18.75±0.05	18.80±0.07	0''/8	0.01	114°	compact
TN J1428+2425	...	K10	K <sub>S</sub>	0.021	>22.1	...	...	...	...	...	non-detection
WN J1433+3044	...	K7	K <sub>S</sub>	0.006	18.37±0.05	17.93±0.04	17.54±0.05	0''/8	0.45	98°	elliptical
WN J1450+3534	...	K10	K	0.004	20.00±0.07	19.67±0.07	18.84±0.07	0''/4	0.28	35°	compact
TN J1506+2728	...	K10	K <sub>S</sub>	0.012	20.59±0.10	20.30±0.12	19.82±0.17	...	...	...	low S/N
WN J1525+3010	...	K7	K	0.007	20.08±0.08	19.51±0.09	19.49±0.18	0''/5	0.06	44°	compact
WN J1550+3830	...	K10	K	0.004	19.15±0.05	18.84±0.05	18.70±0.08	...	0.43	155°	compact
WN J1555+4011	...	K10	K <sub>S</sub>	0.006	18.95±0.05	18.71±0.05	18.90±0.11	0''/4	0.20	130°	compact
WN J1604+5505	...	K10	K <sub>S</sub>	0.003	21.45±0.18	21.67±0.38	20.98±0.51	...	...	...	low $\mu$
WN J1645+4413	...	K10	K <sub>S</sub>	0.005	18.31±0.04	18.07±0.04	17.66±0.05	1''/2	0.48	145°	elliptical
WN J1731+4640	...	K10	K <sub>S</sub>	0.009	19.78±0.07	19.18±0.07	19.08±0.11	...	...	177°	low S/N
WN J1731+4654	...	K10	K <sub>S</sub>	0.009	>21.5	...	...	...	...	...	non-detection
MP J1755-6916	2.551	C2	K	0.027	19.03±0.13	18.28±0.12	17.87±0.17	...	...	...	low $\mu$
MP J1758-6738	2.026	C2	K	0.028	19.20±0.17	18.25±0.14	17.78±0.21	...	...	...	low S/N
WN J1804+3048	...	K10	K <sub>S</sub>	0.021	19.73±0.07	19.55±0.09	19.62±0.19	0''/6	0.05	26°	compact
WN J1818+3852	...	K10	K	0.011	19.91±0.07	19.50±0.07	17.52±0.04	0''/5	0.16	165°	compact
WN J1818+6144	...	K10	K	0.021	17.86±0.04	17.44±0.04	17.01±0.04	0''/5	0.29	12°	elliptical
WN J1836+5210	...	K10	K <sub>S</sub>	0.016	18.24±0.04	17.66±0.04	17.45±0.04	...	0.55	168°	interacting
WN J1911+6342	3.590	K10	K	0.025	20.44±0.09	19.87±0.10	18.57±0.07	...	...	...	low $\mu$
WN J1917+6635	...	K10	K	0.015	20.43±0.09	19.97±0.11	19.84±0.22	...	0.56	176°	extended
MP J1929-3732	0.748	C2	K	0.122	17.59±0.08	17.14±0.07	16.96±0.09	0''/3	...	...	compact
TN J1941-1952	...	K12	K	0.042	18.29±0.04	17.64±0.04	17.90±0.09	...	...	...	compact
TN J1954-1207	...	K10	K	0.053	20.01±0.08	19.86±0.10	19.35±0.14	...	...	...	companions
MP J2003-8340	1.169	C2	K	0.078	18.84±0.12	18.36±0.12	18.63±0.30	1''/3	...	...	compact
TN J2007-1316	...	K12	K <sub>S</sub>	0.044	19.02±0.06	18.84±0.08	17.85±0.08	<0''/3	...	44°	compact
TN J2009-3040	...	K10	K	0.066	18.26±0.04	18.12±0.04	18.05±0.05	0''/1	...	37°	compact/unresolved
TN J2028-1934	...	K12	K <sub>S</sub>	0.023	19.05±0.06	18.49±0.06	18.34±0.10	...	...	...	low S/N
WN J2044+7044	...	K10	K <sub>S</sub>	0.173	19.37±0.06	19.20±0.07	19.90±0.23	0''/4	0.06	1°	compact
MP J2045-6018	1.464	C2	K	0.023	18.28±0.10	17.96±0.11	18.06±0.22	1''/0	...	...	compact
MP J2048-5750	1.262	C2	K	0.025	17.57±0.07	17.22±0.07	17.02±0.09	1''/1	...	...	compact
MP J2126-5439	...	C2	K	0.015	18.12±0.09 <sup>†</sup>	17.77±0.09 <sup>†</sup>	17.53±0.12 <sup>†</sup>	2''/6	...	...	compact
WN J2213+3411	...	K12	K <sub>S</sub>	0.048	18.28±0.05	17.86±0.05	17.45±0.06	0''/4	0.33	140°	compact
MP J2226-7654	...	C2	K	0.051	18.93±0.14 <sup>†</sup>	18.39±0.14 <sup>†</sup>	18.04±0.23 <sup>†</sup>	...	...	...	low S/N
WN J2250+4131	...	K12	K	0.090	19.72±0.07	19.42±0.09	18.89±0.13	<0''/3	...	36°	compact
WN J2313+4253	...	K12	K	0.056	17.70±0.04	16.99±0.03	16.66±0.04	...	...	...	pulsar
TN J2314+2053	...	K12	K	0.100	19.34±0.06	18.90±0.06	18.52±0.09	0''/5	0.28	6°	compact
MP J2352-6154	...	C2	K	0.008	19.30±0.15	18.41±0.12	18.05±0.16	...	...	...	interacting

<sup>a</sup>Extinction in K-band, from H I column densities.

<sup>†</sup>Estimated from non-photometric conditions.

**The individual figures are available on <http://www.strw.leidenuniv.nl/~debreuck/papers/>**

FIG. 2.— Cutout images of the 81  $K$ -band detections. Each image is  $8'' \times 8''$ , and the origin is the position listed with 'IR' in Table 5. The vector next to the name indicates the position angle of the radio source, unless no high-resolution radio map is known. The images are oriented North up and East left.

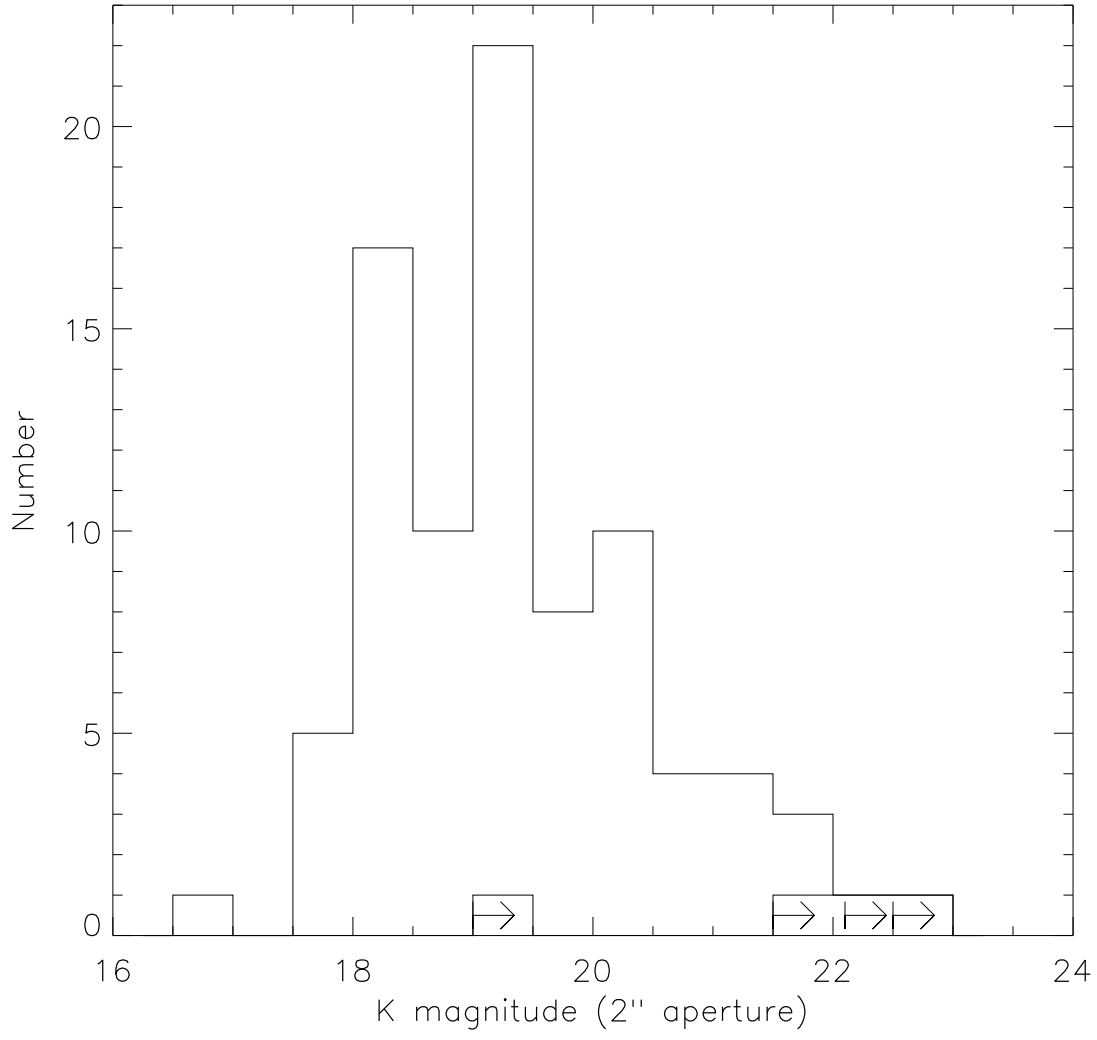


FIG. 3.— Histogram of the  $K$ -band magnitudes measured in a  $2''$  diameter aperture. Non detections are indicated by arrows.

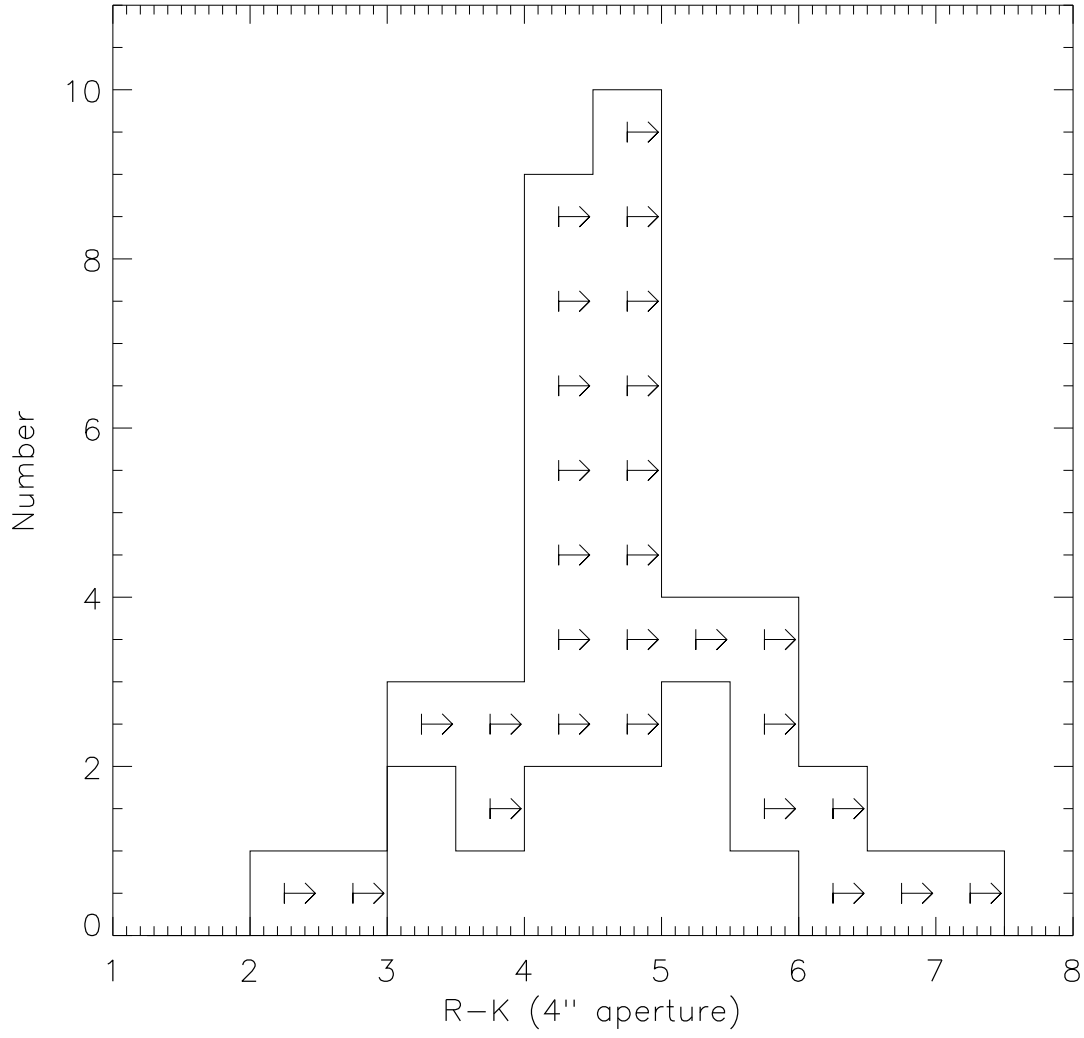


FIG. 4.— Histogram of the  $R - K$  colors measured in a  $4''$  diameter aperture. Non detections in the  $R$ -band are indicated by arrows.

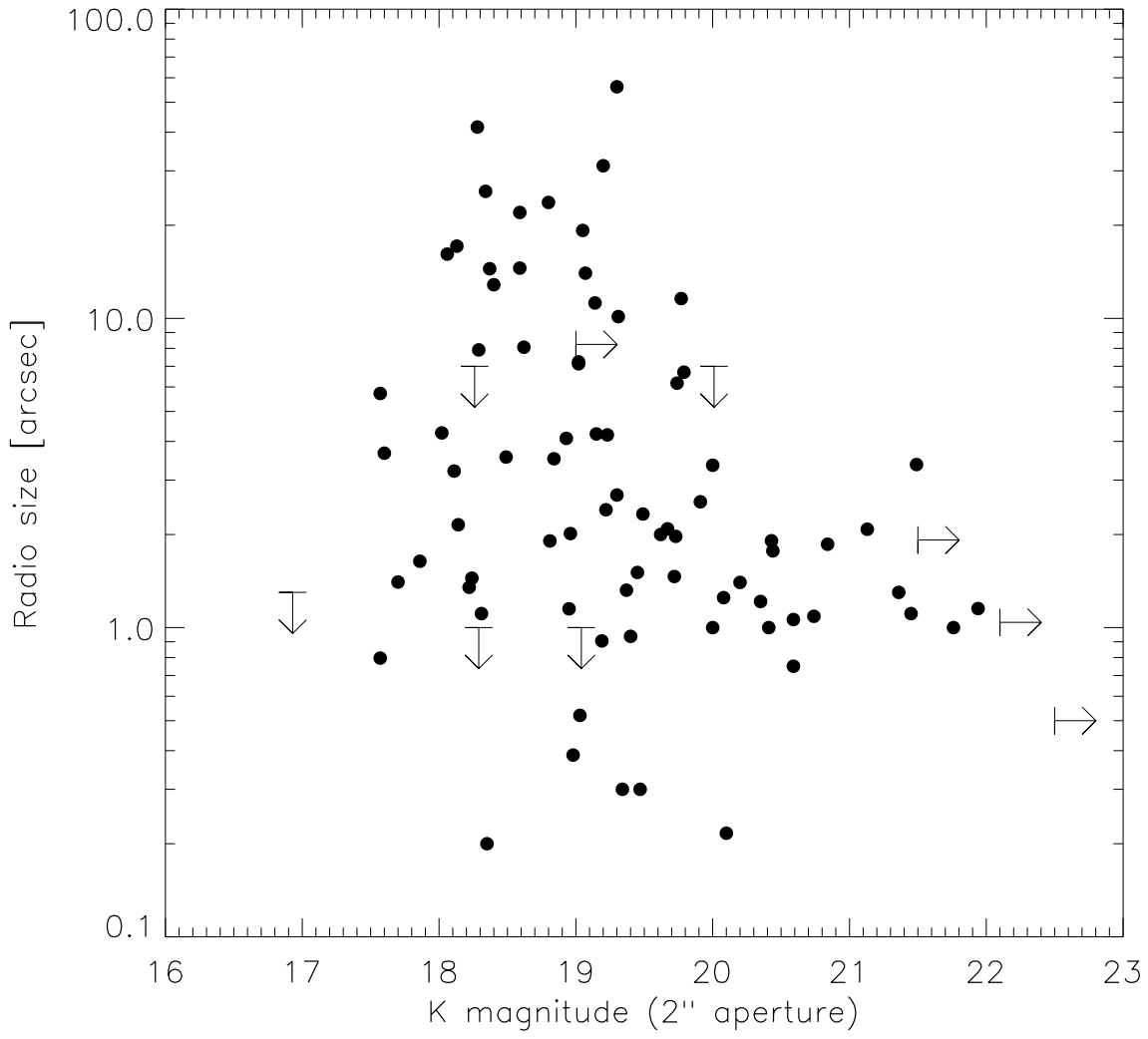


FIG. 5.— Radio largest angular size plotted against  $K$ -magnitude in a  $2''$  diameter aperture. Note that all the  $K > 20$  sources are  $\lesssim 3''$ , while brighter sources have a larger range of sizes.



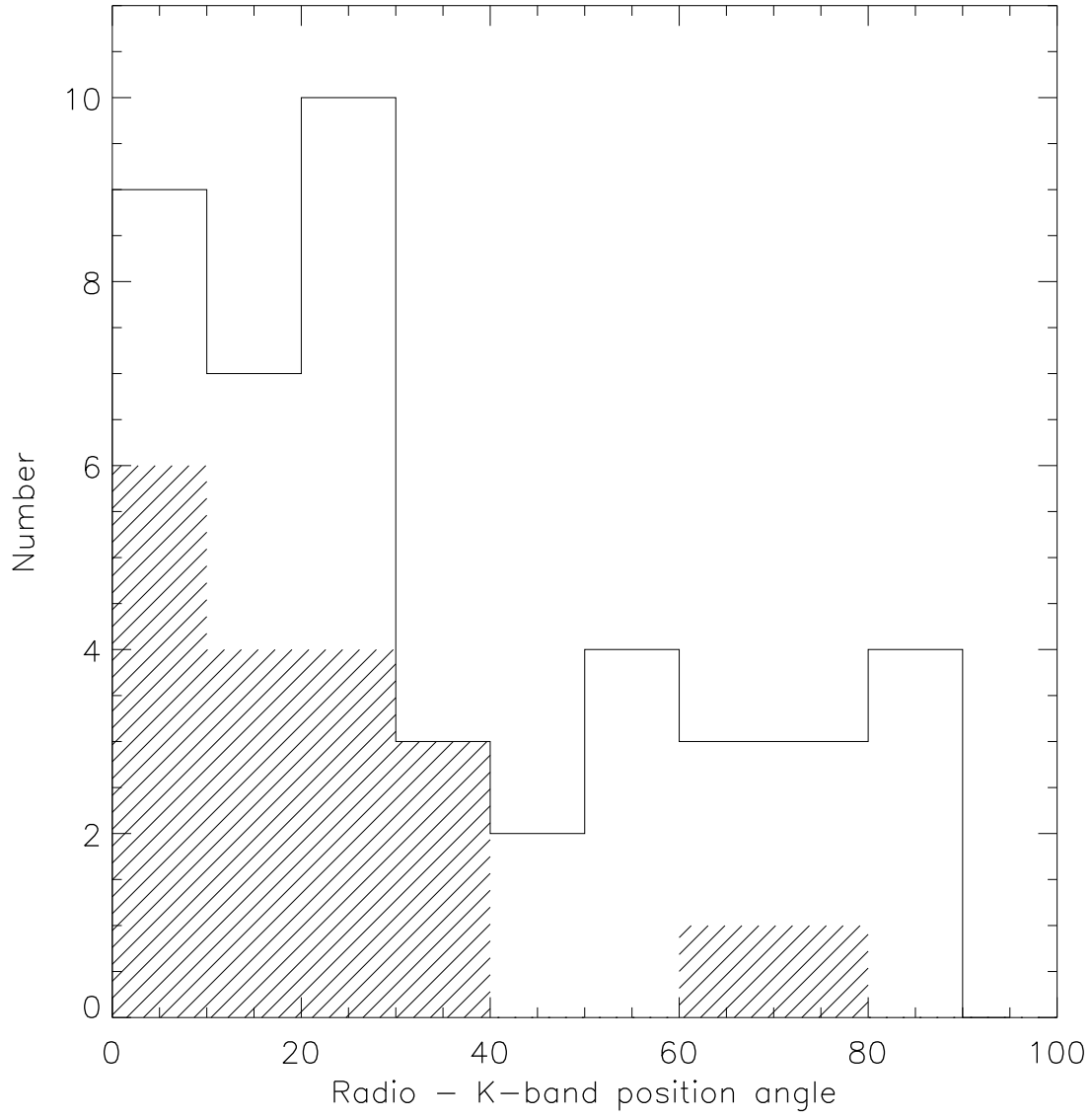


FIG. 6.— Distribution of the differences in position angle between the radio emission and the  $K$ -band emission of our USS sources, measured at the outer isophote of the `ellipse` fitting. The shaded histogram gives the distribution of the sources with radio sizes larger than  $5''$ .

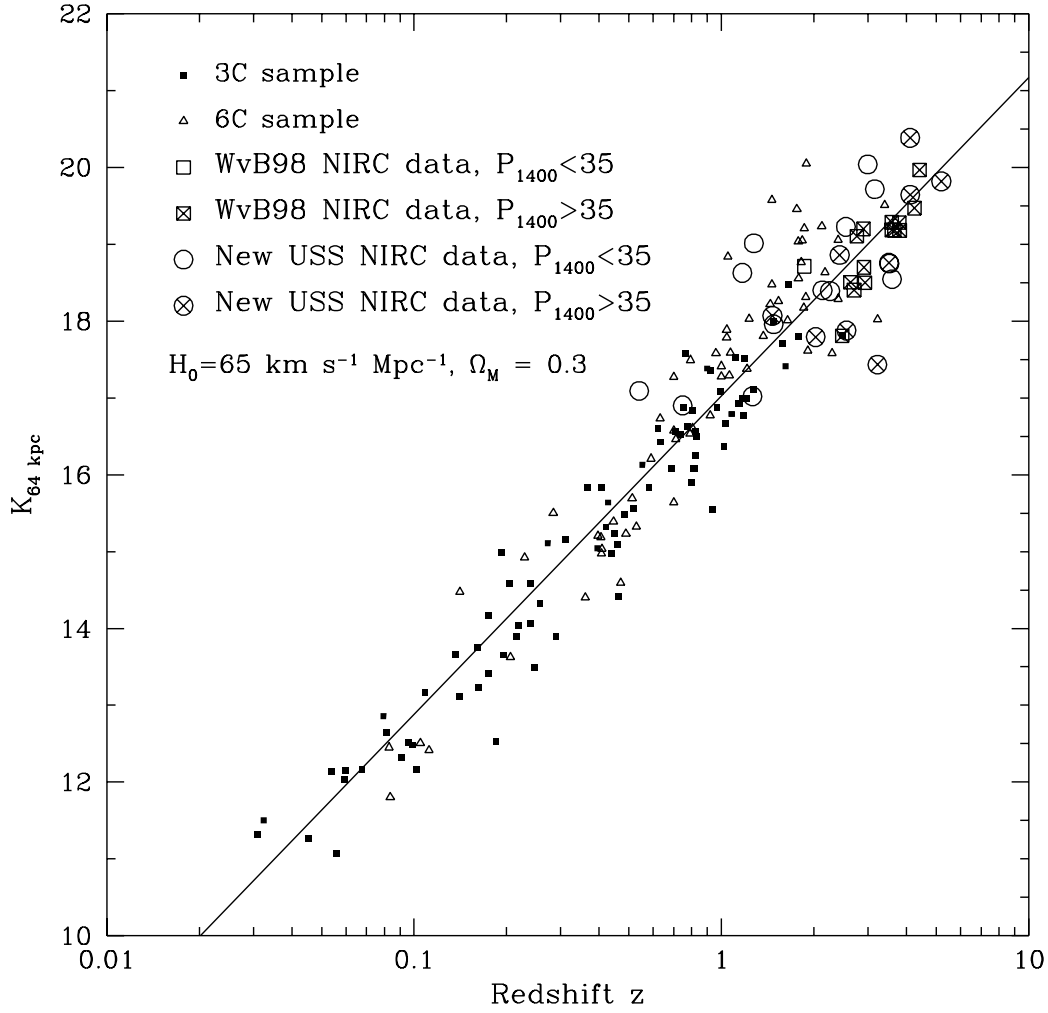


FIG. 7.— Hubble  $K - z$  diagram of radio galaxies. Our new USS NIRC data are plotted in the same aperture corrected 64 kpc metric diameter magnitudes as the literature data from van Breugel et al. (1998) and Eales et al. (1997). The NIRC data of the sources with radio power  $P_{1400} > 10^{35} \text{ erg s}^{-1} \text{ Hz}^{-1}$  are filled with a cross. The line shows a linear fit to the data, but does not have a direct physical meaning.

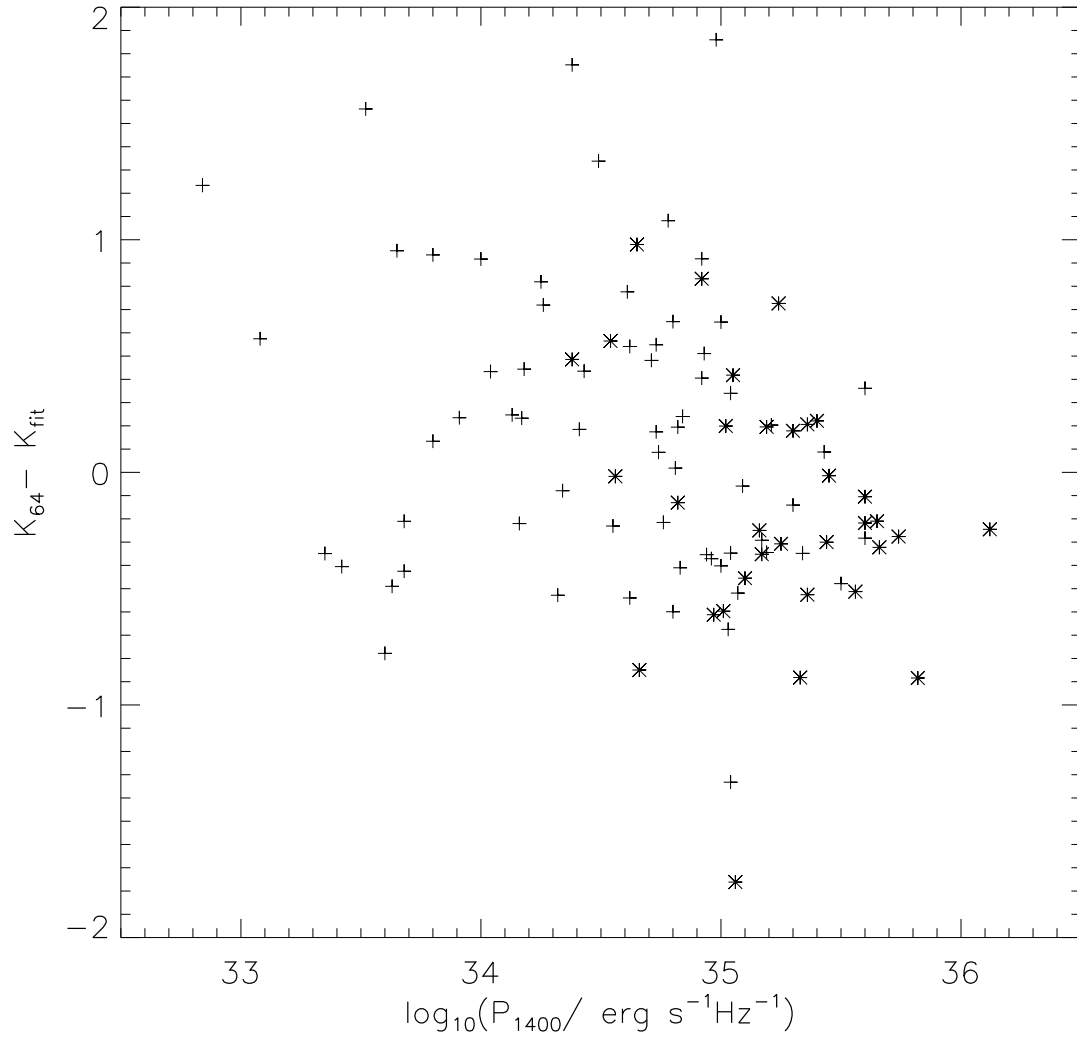


FIG. 8.— Deviation from a linear fit to the  $\log_{10}(z) - K_{64\text{pc}}$  relation plotted against radio power at 1.4 GHz, using the data from Figure 7. Plus-signs represent radio galaxies at  $z < 2$ , stars those at  $z > 2$ . There is a statistically significant (99.94%) trend for the higher luminosity radio sources to have more luminous parent galaxies.

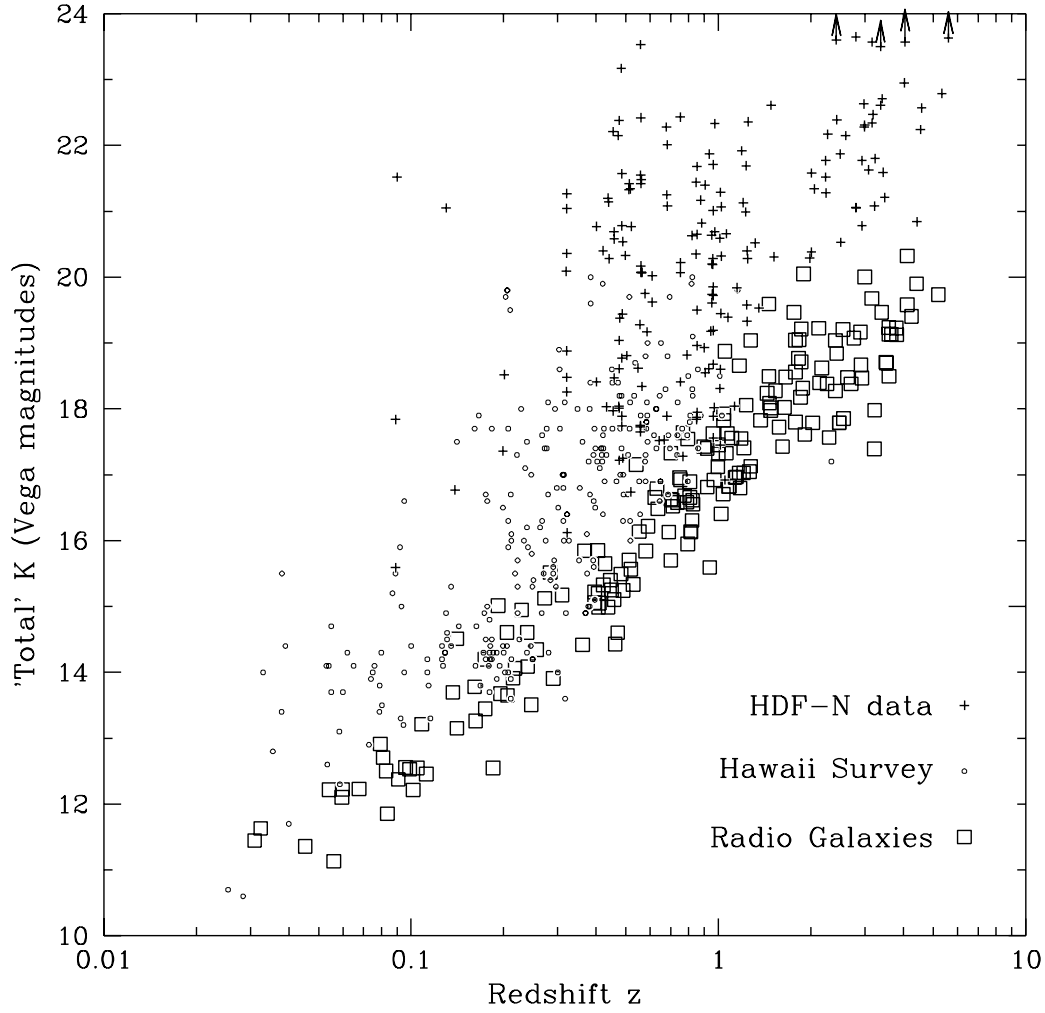


FIG. 9.— Composite Hubble  $K - z$  diagram of radio-loud and radio-quiet galaxies. The radio-loud data are the same as in Figure 7; the radio-quiet data are taken from the HDF-North and the Hawaii survey. The radio-quiet galaxies do not show the strong correlation seen in radio-loud galaxies, and are significantly fainter than the radio-loud galaxies, which trace the bright envelope of the radio-quiet data at  $z \lesssim 1$ , and are  $\gtrsim 2$  magnitudes brighter at  $z \gtrsim 1$ .

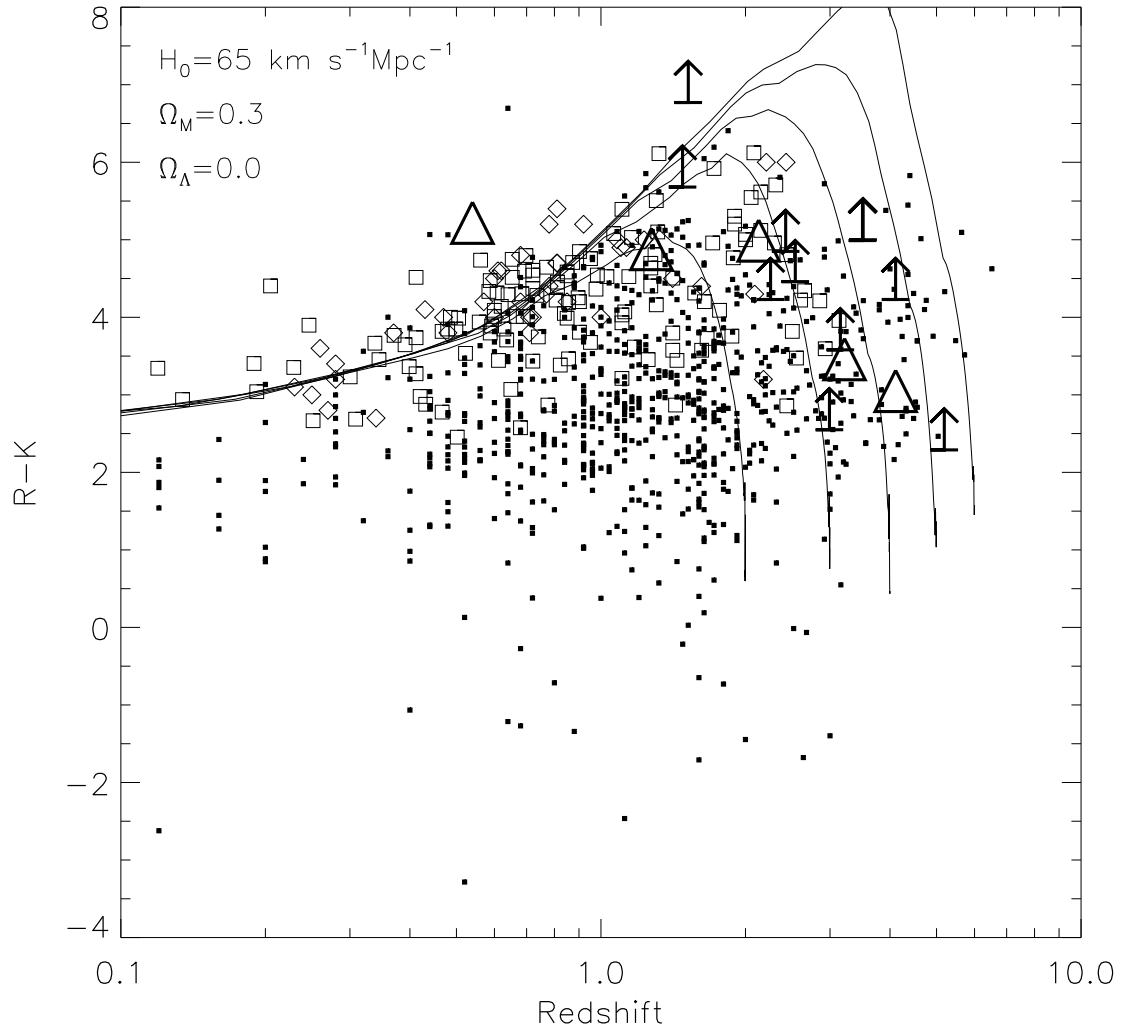


FIG. 10.—  $R-K$  color plotted against redshift. Small squares are optically selected galaxies from the HDF-North with photometric redshifts (Fernández-Soto, Lanzetta, & Yahil 1999). Open squares and diamonds are radio galaxies from the MRC sample of McCarthy (1999) and the 7CRS of Willott, Rawlings & Blundell (2001b). Large triangles and lower limits are galaxies from our USS sample. The solid lines show the color evolution of a galaxy formed in an instantaneous burst at  $z_{form} = 2, 3, 4, 5, 6$ , calculated using the PEGASE 2 code.

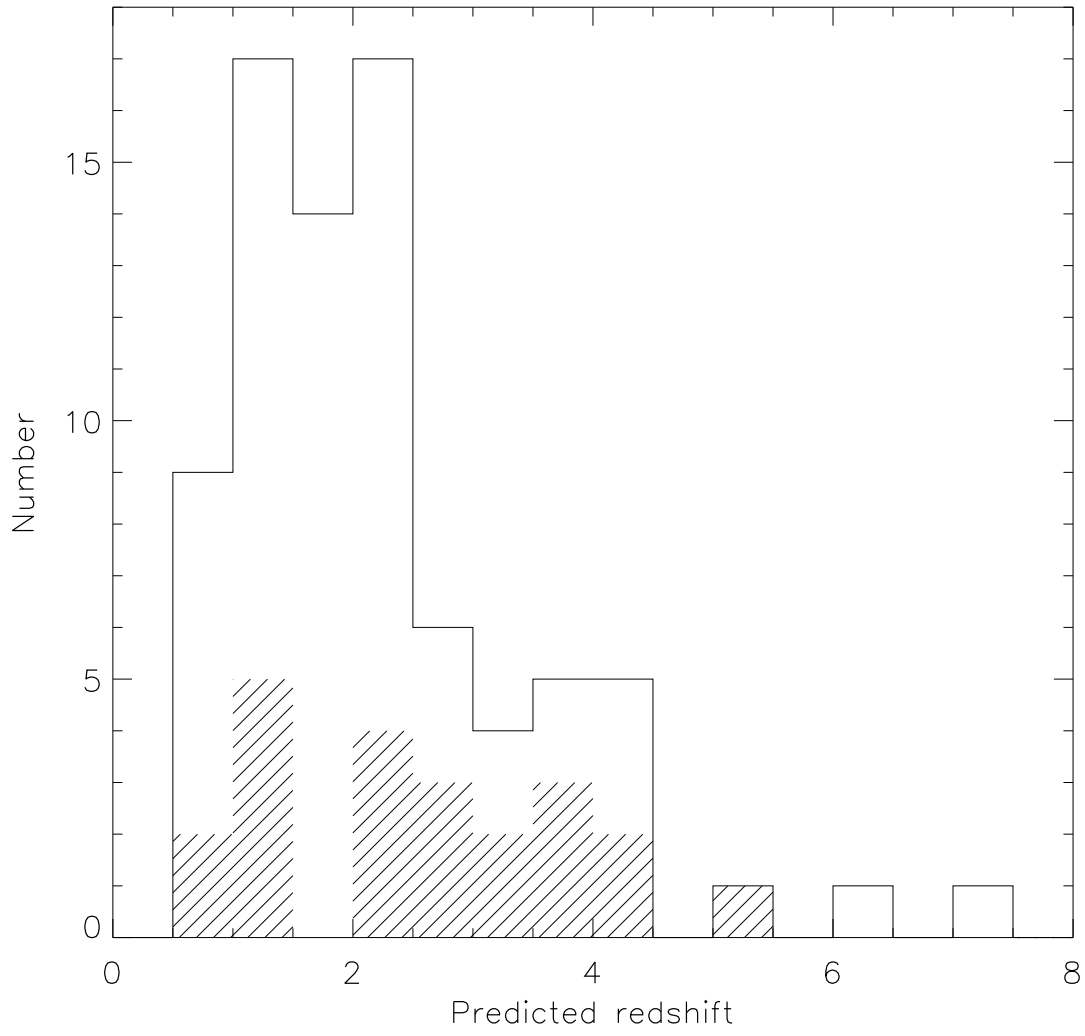


FIG. 11.— Predicted redshift distribution of the 80 objects with  $K$ -band detections. The redshifts are estimated from the  $K - z$  diagram in Figure 7. The shaded histogram shows the distribution of the 22 objects with spectroscopic redshifts from this sample.

## APPENDIX

**The individual figures are available on <http://www.strw.leidenuniv.nl/~debreuck/papers/>**

FIG. 12.— Finding charts for all 128 object observed. We show the near-IR image if obtained, otherwise the optical image, as indicated above each figure. Each image is  $90'' \times 90''$ . The circled star labeled 'A' is the offset star, whose coordinates are listed in Table 5. The position of the radio centroid is indicated with an open crosshair.